The Influence of Eddies on Tracer Transport in the Abyssal Ocean

CAROL LADD AND LUANNE THOMPSON

School of Oceanography, University of Washington, Seattle, Washington

(Manuscript received 16 December 1996, in final form 1 December 1997)

ABSTRACT

Tracer transport mechanisms in a deep western boundary current (DWBC) are explored using a three-layer, eddy-resolving quasigeostrophic model. The model is forced with a steady, sinusoidal wind stress. The effects of the wind stress, coupled with instabilities, create an unsteady, zonal surface jet at the boundary between the model subtropical and subpolar gyres. The bottom layer includes a DWBC created by specifying a mass inflow at the northern boundary and a mass outflow at the southern boundary. A numerical tracer is introduced into the DWBC with the mass source at the northern boundary.

The surface jet creates an effective boundary to tracer transport in the DWBC. This barrier to meridional tracer transport causes approximately 70% of the tracer moved out of the northern part of the DWBC to be transported zonally into the interior with only 30% continuing southward in the DWBC. In model runs with a flat bottom, approximately 20% of the total meridional tracer flux is due to the eddy field. When the model is run with sloping topography along the western boundary, only 2% of the meridional tracer flux is due to the eddy field. The dependence of zonal tracer flux on eddies is highly latitude dependent, and in the region of interest (far from the northern boundary) the mean field is responsible for most of the zonal tracer flux.

Eddies play a role in tracer flux in two ways: 1) the direct influence of the eddies in transporting tracer and 2) the effect of the eddies in driving the mean flow. A comparison between eddy-resolving runs and those with eddy diffusivity to parameterize the eddies suggests that the role of the eddy field in driving the mean flow field is of primary importance.

1. Introduction

A large part of the thermohaline circulation in the North Atlantic consists of the northward flowing, warm, salty Gulf Stream overlying the southward flowing, cold, dense deep western boundary current (DWBC). The DWBC originates with deep convection in high latitudes, overflows sills at the Denmark Straits overflow and the Iceland–Scotland overflow, and flows southward along the western boundary of the Atlantic. Due to its convective origins, the DWBC contains the signature of various tracers including an oxygen maximum (Wust 1935), a tritium (^{3}H) maximum (Jenkins and Rhines 1980), and high concentrations of the chlorofluoromethanes F-11 and F-12 (e.g., Gammon and Bullister 1982; Smethie and Trumbore 1984; Fine and Molinari 1988).

Numerous tracer studies (both numerical and observational) have been used to study the DWBC (e.g., Spall 1996; Pickart 1992; Pickart and Smethie 1993; Rhein 1994; Pickart and Hogg 1989). In particular, considerable attention has been paid to the region where the DWBC crosses under the Gulf Stream. This region is particularly interesting because it is a confined region through which much of the thermohaline circulation passes. Thus, an improved understanding of the DWBC/Gulf Stream system is necessary to our understanding of the ocean's role in the global climate system.

Although the Gulf Stream system in the North Atlantic is probably the most thoroughly studied region in the World Ocean, the deep flow in this region is still only partially explored. Estimates of age based on tracer measurements imply a DWBC advection speed of 1–2 cm s^{-1} (Doney and Jenkins 1994; Pickart et al. 1989), whereas direct measurements give speeds of 5–20 cm s^{-1} (Pickart and Smethie 1993; Watts 1991; Fine and Molinari 1988). This difference in estimated DWBC speed has been attributed to mixing and exchange with the interior.

The studies referenced above concentrate on various aspects of the DWBC in general and tracer transport in particular. Pickart and Hogg (1989) use a model consisting of a simplified gyre, representing the northern recirculation gyre of the deep Gulf Stream, next to a deep boundary current to study the transfer of tracer via diffusion from the boundary current to the recirculation gyre. The tracer is introduced into the boundary current and diffuses into the interior, becoming entrained in the gyre. By applying their model results to the observed oxygen distribution in the DWBC/Gulf Stream region,

Corresponding author address: Ms. Carol Ladd, School of Oceanography, University of Washington, Box 357940, Seattle, WA 98195-7940.
E-mail: cladd@ocean.washington.edu

they deduce estimates of lateral and vertical diffusivity ($\kappa \sim 10^6$ cm^2 s^{-1}, $\nu \sim 10$ cm^2 s^{-1}).

Spall (1996) uses a primitive equation model with three layers to model the Gulf Stream/DWBC crossover region. He introduces a DWBC in both the second and third layers (the ''upper'' and ''lower'' DWBCs) and finds that the upper core of the DWBC (in layer 2) splits into two mean paths as it crosses under the model Gulf Stream. One path flows toward the south along the western boundary while the other is turned offshore under the Gulf Stream. The lower DWBC (in layer 3) continues to flow along the western boundary with very little interaction with the interior. Spall also finds that the strength of the Gulf Stream has a direct impact on the strength of interaction between the upper DWBC and the interior.

Using CFC tracer data from a 1990 hydrographic survey, Pickart and Smethie (1993) also find that the behavior of the DWBC is depth dependent. They find that the shallow component of the DWBC (approximately 500–1200 m) is sheared in half as it crosses under the Gulf Stream. The shallow sublayer is turned offshore as it crosses under the Gulf Stream while the onshore-most portion of the deeper sublayer continues southward along the boundary with its CFC signal intact. Both sublayers of the shallow DWBC show recirculations as they cross under the Gulf Stream, but the recirculated transport is immediately replenished by inflow from the interior. Thus, at the crossover, there is no substantial drop in transport, just a severe altering of the water properties. The DWBC becomes noticeably warmer and saltier and its CFC content is decreased.

In this study, we have used a highly idealized model to examine the structure of the time-dependent eddy field and the effects of that structure on tracer movement in the DWBC as it crosses under a surface jet. In addition, we have explored the role of variable bottom topography in modifying the eddy structure and thus the eddy-induced tracer fluxes.

This paper is organized as follows. In section 2, a description of the numerical model is given. Section 3 contains a description of the results obtained with the model, including descriptions of the mean streamfunction fields, the meridional and zonal tracer fluxes and tracer transport mechanisms, a discussion of the lateral diffusivity parameterization, and results from tests using various eddy diffusivity formulations. Conclusions are presented in section 4.

2. Model description

The model used for this study traces its roots to the two-layer eddy-resolving quasigeostrophic model first used by Holland (1978). The current version of the model has three layers and a stretched grid in the east–west direction. The stretched grid provides enhanced resolution adjacent to the western boundary with a minimum grid spacing of approximately 4 km at the western wall expanding gradually to 20-km grid spacing in the interior. The enhanced resolution on the western boundary is necessary in order to resolve the smaller scales inherent in western boundary dynamics. The meridional grid spacing is uniformly 20 km. Table 1 contains a list of the model parameters and Fig. 1 is a schematic of the structure of the model. See Lozier and Riser (1989) for a discussion of the model equations and parameters.

TABLE 1. Model parameters.

Basin dimensions	4000 km × 4000 km
Layer thicknesses	$H_1 = 300$ m, $H_2 = 700$, $H_3 = 4000$ m
Total ocean depth	$H = 5000$ m
Reduced gravity	$g'_{12} = 0.03$ m s^{-2}, $g'_{23} = 0.02$ m s^{-2}
Coriolis parameters	$f_0 = 9.3 \times 10^{-5}$ s^{-1}, $\beta = 2 \times 10^{-11}$ m^{-1} s^{-1}
Lateral dissipation coefficient	
High-resolution model runs	$\nu = 1 \times 10^2$ m^2 s^{-1}
Low-resolution model runs	$\nu = 2 \times 10^4$ m^2 s^{-1}
Bottom friction coefficient	$\varepsilon = 1 \times 10^{-7}$ s^{-1}
Wind stress	$\tau = (-\tau_0 \cos(2\pi y/L)/\rho_0, 0)$ cm^2 s^{-2}
Wind stress amplitude	$\tau_0 = 1$ dyn cm^{-2}
Mean state density	$\rho_0 = 1$ g cm^{-3}
Rossby radii of deformation:	
First baroclinic	$l_1 = 47$ km
Second baroclinic	$l_2 = 20$ km
Stretched coordinate	$\xi(x) = x + a\lambda(1 - \exp(-x/\lambda))$ for $\lambda = 200$ km, $a = 4$
Topography	$H(x) = H_0 \exp(-x/L)$ for $H_0 = 1000$ m, $L = 500$ km

a. Deep western boundary current

The only differences between the model used here and the model used by Lozier and Riser (1989) are the presence of topography (discussed below) and the inclusion of a DWBC in the third layer. The DWBC was created by specifying a streamfunction on the northern and southern boundaries in the deepest layer, taking into account mass conservation requirements of quasigeostrophic theory as outlined by McWilliams (1977). The following streamfunction was specified on the northern and southern boundaries in the deepest layer:

$$\psi_3(x) = Ae^{-x/L}\left(\frac{x}{2L} + 1\right)$$

$$\text{at } y = 0 \quad \text{and} \quad y = 4000 \text{ km},$$

where $A = 5000$ m^2 s^{-1} is the amplitude, and $L = 40$ km is the decay scale of the boundary current. The DWBC has a Munk layer structure with potential vorticity dissipation in the western boundary layer dominated by lateral friction. This results in a DWBC with

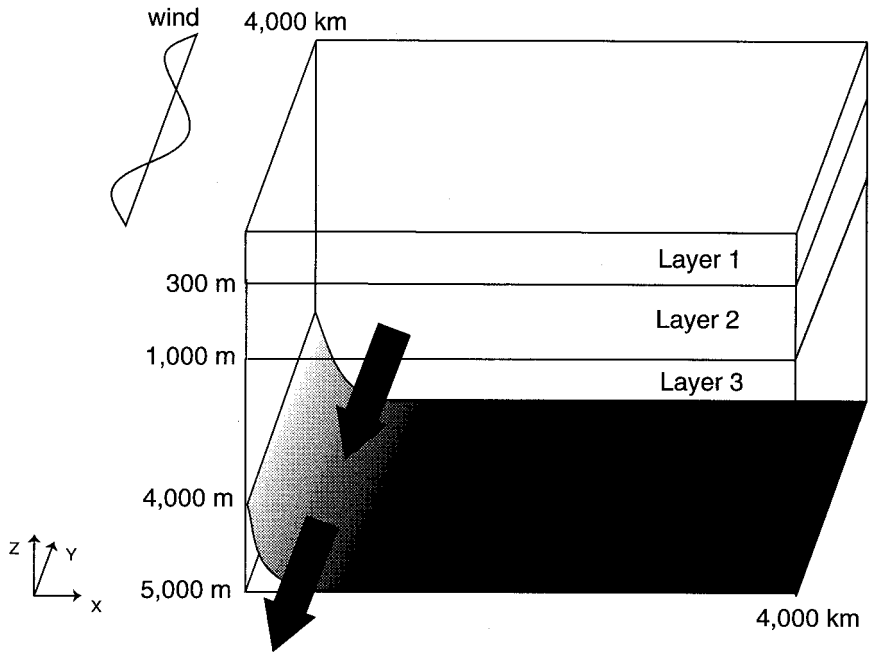

FIG. 1. A schematic diagram for the structure of the model.

a characteristic western boundary width of $\delta = (\nu/\beta)^{1/3} = 17$ km, approximately half of the decay scale L of the boundary condition.

The DWBC streamfunction satisfies free slip boundary conditions on all walls with the additional boundary conditions $\psi_3(x = 0 \text{ km}) = A$ and $\psi_3(x = 4000 \text{ km}) = 0$, for all y. Thus, meridional mass transport in layer 3 is constant. For the upper two layers, a no-flow ($\psi_{1,2} = 0$) boundary condition was applied on all boundaries.

The resulting DWBC southward speed ($v = \partial\psi_3/\partial x$) is 6.25 cm s^{-1} at the western boundary, decaying to 1.15 cm s^{-1} at $x = 100$ km. Once the DWBC leaves the northern boundary, it shrinks to the characteristic western boundary width δ mentioned above. When the effects of the surface wind forcing are included, the region of southward flow is approximately 50 km wide with southward speeds varying between roughly 20 cm s^{-1} at the western boundary and 0 cm s^{-1} at $x = 50$ km in the subpolar gyre. The southward speed of the DWBC averaged over the westernmost 50 km and the northern half of the model basin is approximately 10 cm s^{-1}. These values are consistent with those observed for the North Atlantic DWBC (Pickart and Smethie 1993; Watts 1991; Fine and Molinari 1988). The total meridional mass transport is 20 Sv and is primarily carried in the DWBC.

b. Wind forcing

The surface layer is forced with a steady sinusoidal wind stress. The effects of the wind stress, coupled with baroclinic and barotropic instabilities, create an unsteady, zonal surface jet at the boundary between the model subtropical and subpolar gyres.

c. Topography

Numerical experiments are run with both variable depth and flat bottom conditions. For variable depth runs, the bottom topography consists of a sloping exponential along the western boundary. Topography (in meters above the bottom) is described by the following equation:

$$H(x) = H_0 e^{-x/L},$$

where $H_0 = 1000$ m and $L = 500$ km. This sloping exponential along the western boundary is similar to the structure of the continental rise along the western boundary of the North Atlantic in many places (see Fig. 4 of Doney and Jenkins 1994 for example).

d. Tracer

To model tracers, such as CFCs and tritium, seen in the DWBC of the North Atlantic, a steady flux of tracer into the basin is maintained in the DWBC inflow in the third layer of the model domain. This tracer acts like CFC concentration in that there is no decay timescale to the tracer. A constant tracer concentration in the form of a Gaussian centered at $x = 0$ km with a magnitude of 1.0 and a decay scale of 50 km is maintained as a boundary condition at the northern boundary at the northwest corner of the model basin. The tracer is ad-

vected into the model domain by the DWBC inflow with the following equation:

$$\frac{\partial T}{\partial t} + \mathbf{u}\cdot\nabla T = \nabla\cdot(\kappa\nabla T),$$

where T is the tracer concentration and κ is the diffusion coefficient. For the high-resolution model runs discussed in section 3a–c, the diffusion coefficient κ is kept at zero. The effects of a nonzero diffusion coefficient in low-resolution model runs as an attempt to parameterize the effects of eddies on tracer transport is discussed in section 3e.

Once the model has run for a sufficient time that tracer has reached the southern boundary, tracer is advected out of the model domain with the DWBC outflow. Except at the DWBC inflow and outflow, there is a no-flux boundary condition for both tracer and mass. A positive definite advection scheme by Smolarkiewicz (1983) that attempts to minimize numerical diffusion is used to advect the tracer. This scheme has fairly low computational cost as compared to other positive definite schemes.

3. Results

The model was initialized at rest and spun up for approximately ten years before any tracer was introduced. After spinup, a continuous flux of tracer was introduced into the basin with the DWBC. The model was then integrated with the constant tracer influx for 5000 days (about 13.7 yr). This compares to a CFC age in the DWBC of roughly 8 yr at 55°W north of the crossover region (Pickart et al. 1989). The model was run both in a flat-bottom configuration and with topography (as explained above).

a. Mean fields

The time-averaged streamfunction fields for the flat-bottom and the topography configurations (Figs. 2 and 3) were calculated over 1000 days, subsampled every 2 days. The mean streamfunction was calculated over both shorter and longer periods for comparison and was essentially the same in all cases, demonstrating that the 1000-day mean had reached equilibrium.

The standard wind-driven double gyre, including Sverdrup interior flow, a western boundary current, and a midbasin eastward-flowing jet, is seen in the surface layer of both the flat-bottom and the topography runs. In both the flat-bottom and the topography configurations, the transport in each gyre in the first layer is

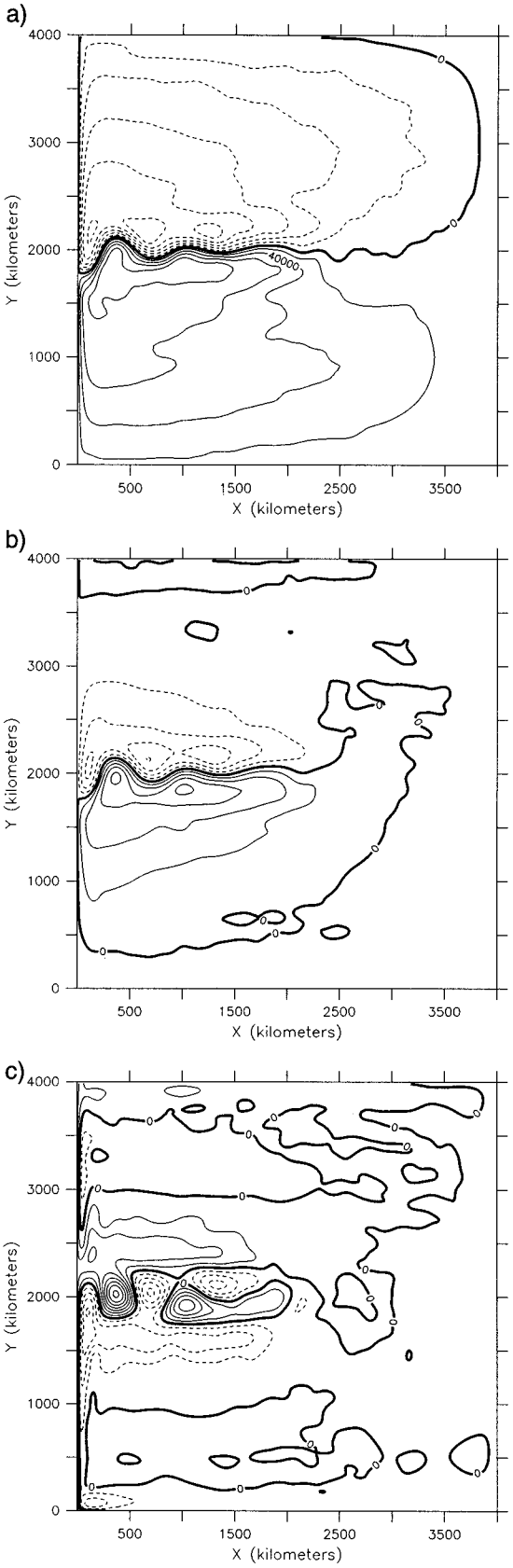

→

FIG. 2. Time-averaged streamfunction fields for the flat-bottom configuration. (a) Layer 1 (contour interval = 20 000 m² s⁻¹); (b) layer 2 (contour interval = 10 000 m² s⁻¹); (c) layer 3 (contour interval = 2000 m² s⁻¹).

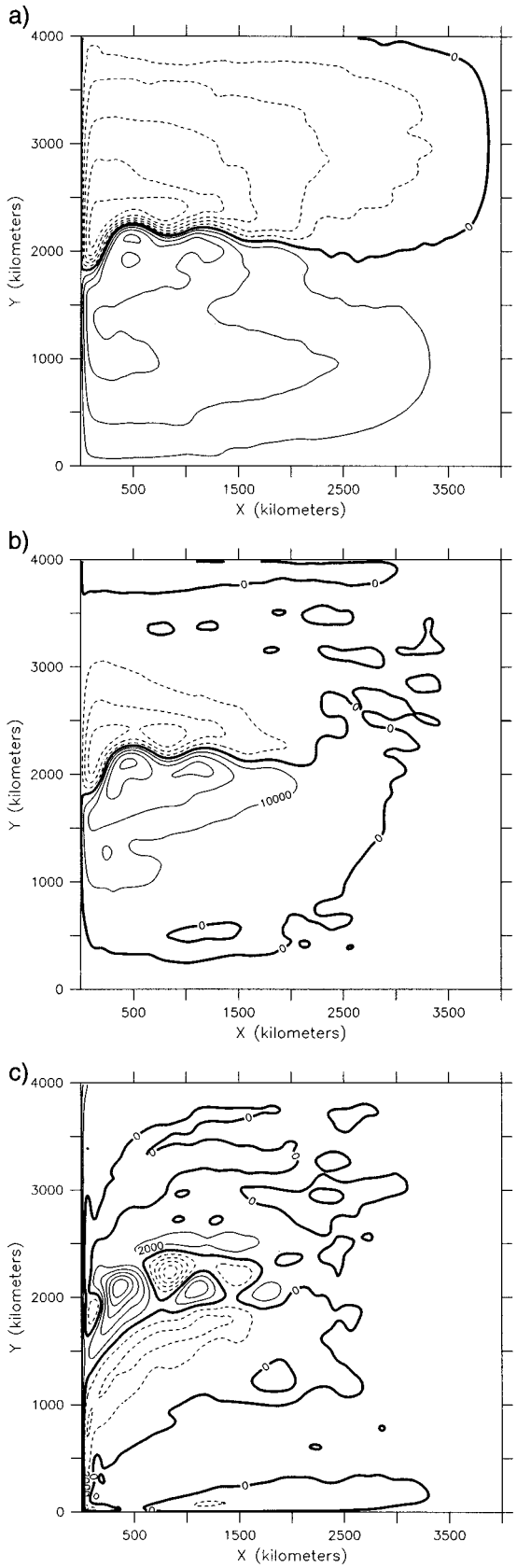

approximately 20–25 Sv (Sv $\equiv 10^6$ m^3 s^{-1}). (The imposed wind stress curl implies a Sverdrup transport of approximately 30 Sv.) The mean western boundary current speeds averaged over the westernmost 100 km are about 60 cm s^{-1} in both configurations. Due to the effects of the DWBC in the third layer, the surface jet separates from the western boundary approximately 200 km south of midbasin. This southern separation point is consistent with findings by Thompson and Schmitz (1989). They demonstrated in a two-layer primitive equation model that the location of the Gulf Stream separation point is shifted southward by the presence of a DWBC. In the absence of the DWBC, the eastward jet separates from the western boundary at exactly midbasin (see Fig. 3 of Lozier and Riser 1989).

The second layer of the model shows weaker gyres with transports of about 15 Sv each (for both flat bottom and topography). In the third layer, the eastward flowing jet (apparent only in the time mean; see Fig. 9 for an example of the instantaneous streamfunction) shows meanders with zonal and meridional scales of several hundred kilometers due to the symmetry-breaking effects of the DWBC. Similar meanders in the abyssal layer have been observed by Rhines and Schopp (1991) due to a nonsymmetric tilted wind field and by Thompson (1995) due to topography. Any of these model features (DWBC, nonsymmetric wind field, or topography) seem to break the symmetry of the double wind-driven gyre in similar ways. Further analysis of this phenomenon is beyond the scope of this paper.

The maximum speed of the current in the meanders is approximately 11 cm s^{-1} in the flat-bottom configuration and 5 cm s^{-1} in the topography configuration as compared with a maximum DWBC speed (right at the western boundary) of about 20 cm s^{-1} (in both configurations) in the time mean. In the absence of a DWBC, the eastward flowing jet in the third layer of the flat bottom configuration is very zonal with almost no meandering (see Fig. 3 of Lozier and Riser 1989).

The effects of topography are almost entirely confined to the third layer. In the flat-bottom configuration, the orientation of the third-layer gyres is primarily zonal. In the third layer of the topography configuration, the gyres are pulled to the south along the western boundary following contours of f/h.

Topography also affects the potential vorticity (PV) of the third layer (Fig. 4). In the flat-bottom case, PV in the third layer is dominated by planetary vorticity, while in the topography case the affects of bottom topography on the stretching term serve to deform the PV contours. In both cases, PV is noticeably affected by

←

FIG. 3. Time-averaged streamfunction fields for the topography configuration. (a) Layer 1 (contour interval = 20 000 m^2 s^{-1}); (b) layer 2 (contour interval = 10 000 m^2 s^{-1}); (c) layer 3 (contour interval = 2000 m^2 s^{-1}).

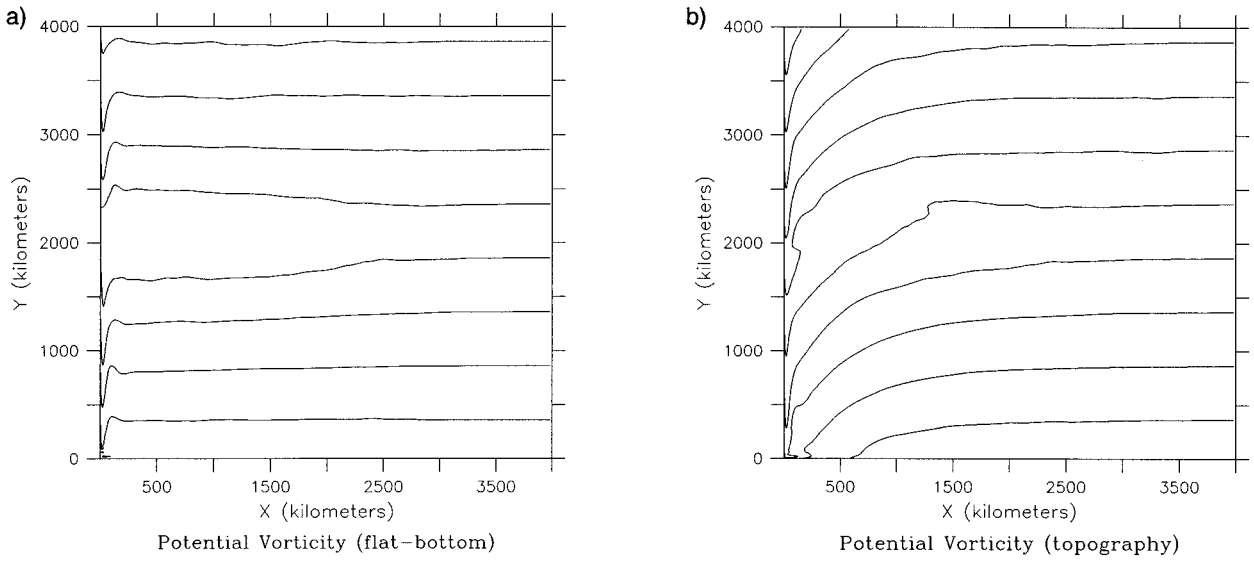

FIG. 4. Time-averaged potential vorticity in layer 3 (contour interval = 1.0×10^{-5} s^{-1}). For (a) flat-bottom configuration and (b) topography configuration.

variations in relative vorticity only along the western boundary. Thus, except at the western boundary, potential vorticity in the third layer can be estimated quite accurately by f/h.

An expansion of the westernmost part of the third layer (Fig. 5) shows the details of the western boundary current. In the flat-bottom configuration, the mean DWBC almost completely turns offshore (at approximately $y = 2500$ km) while in the topography configuration, the mean DWBC is able to remain on the western boundary and continue southward as it crosses under the surface jet. This is because, in the topography configuration, the DWBC is able to conserve potential vorticity by moving up the slope to partially offset the reduction in the Coriolis parameter as it flows southward. In the flat-bottom configuration, the DWBC does not have a slope to move up and thus turns offshore in an attempt to conserve potential vorticity. This is illustrated by examining the meridional gradient of PV (Fig. 6). In the flat-bottom configuration, a maximum in the meridional gradient is apparent at approximately $y =$ 2400–2500 km (the same place where the streamfunction turns offshore). The meridional gradient of PV for the topography case has local maxima with smaller values farther from the western boundary at approximately $y = 2000$ km and $y = 1500$ km. These maxima correspond to latitudes with enhanced eastward flow in the mean streamfunction of the topography configuration. The effect of topography on the potential vorticity dynamics is consistent with findings by Spall (1996). He notes that the lack of a continental slope allows eddy-induced recirculation gyres to develop adjacent to the western boundary and thus maximizes their interaction with the DWBC.

b. Meridional tracer flux

As explained in section 2, a steady influx of tracer is introduced into the model basin with the DWBC in the northwest corner. Once the tracer enters the basin, it is advected by the instantaneous flow. After a 5000-day model run, the tracer is still far from equilibration: more tracer is entering the model at the northern source than is leaving in the south. Since the boundary conditions are no flux away from the inflow and outflow of the DWBC, the model basin would eventually fill with tracer if the model were run long enough. However, this eventual equilibration of tracer would not be representative of real tracers in the ocean because the flow is confined to layers and not all sources and sinks of tracer are included in the model. In this study, because we are concentrating on tracer kinematics in the DWBC, we are not particularly concerned about tracer equilibration in the interior.

One striking feature of the tracer contours at the end of a 5000-day run (Fig. 7) is the lack of significant amounts of tracer south of the midbasin f/h contour. This indicates an effective barrier to meridional transport of tracer across this f/h contour. The barrier can be explained in terms of potential vorticity conservation. The surface jet causes the thickness of the upper layer to increase, thus causing a decrease in the thickness of the lower layers. In order to maintain a constant layer thickness, the southward flowing DWBC has to turn offshore as it crosses under the surface jet (Hogg and Stommel 1985; Spall 1996).

We define a region (A) bounded by the midbasin f/h contour on the south and $x = 200$ km on the east and calculate tracer fluxes out of this region to estimate the strength of the f/h barrier. The total flux out of this

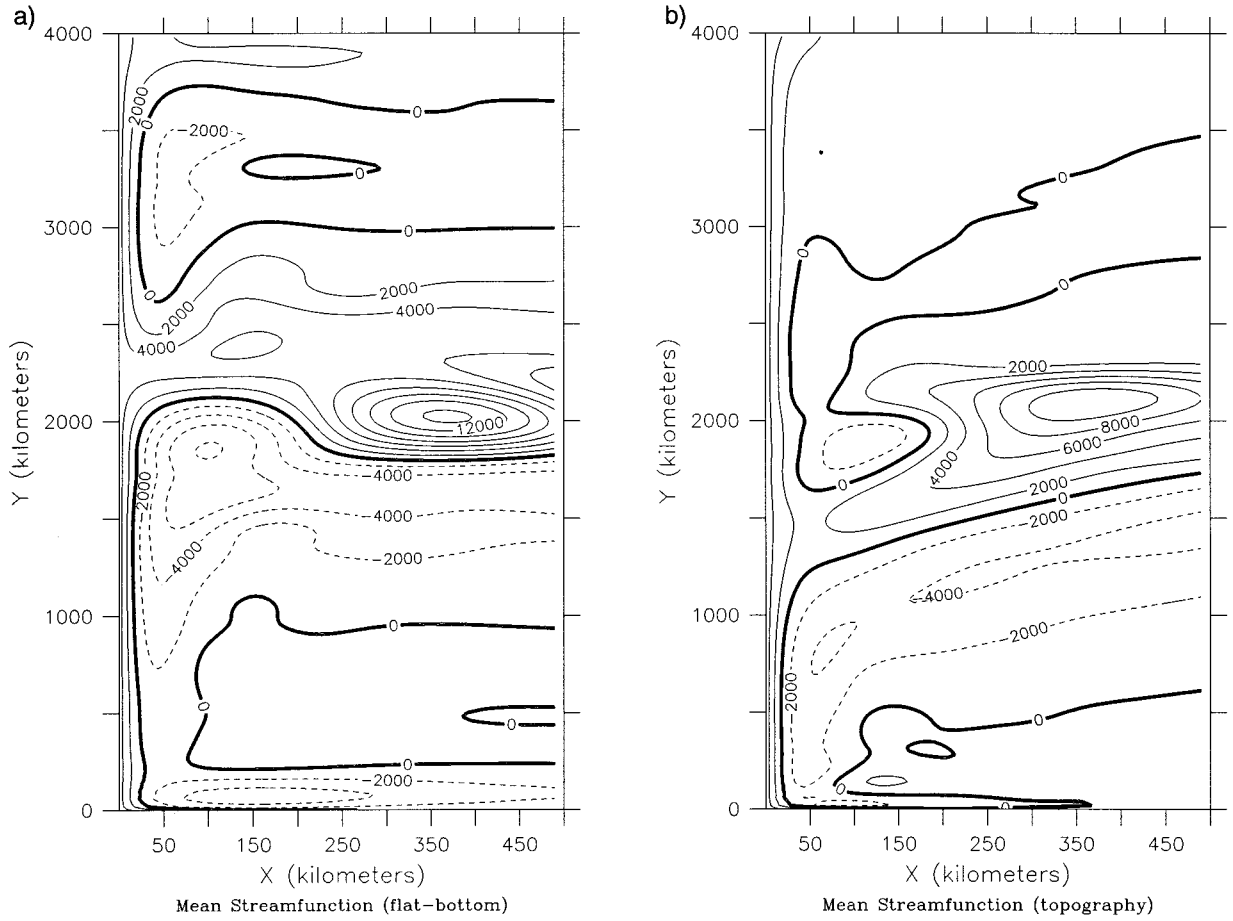

FIG. 5. Time-averaged streamfunction fields for the westernmost 500 km of the third layer (contour interval = 2000 $m^2 s^{-1}$). For (a) flat-bottom configuration and (b) topography configuration.

region is equal to the sum of the meridional flux across the f/h contour between $x = 0$ km and $x = 200$ km and the zonal flux across $x = 200$ km between $y = y_{f/h}$ and $y = 4000$ km. Thus, one measure of the strength of the barrier is the ratio of zonal tracer flux into the interior to total tracer flux out of the region. The first 1000 days of the model run are ignored in the following averages to account for the fact that it takes some time for the tracer to reach the midbasin f/h contour. In the flat-bottom case, the zonal tracer flux across $x = 200$ km integrated from $y = 2000$ km to $y = 4000$ km averaged over the final 4000 days of the 5000-day model run is 1533 kg s^{-1} (if tracer is measured in kg). The meridional tracer flux across $y = 2000$ km integrated from $x = 0$ km to $x = 200$ km averaged over the final 4000 days is 740 kg s^{-1}. Thus, the ratio of zonal flux to total flux is 0.67. Approximately 70% of the total tracer flux out of Region A is into the interior, while only 30% crosses the f/h contour (in the DWBC) into the southern half of the basin. In the topography case, the numbers are slightly different (zonal tracer flux = 1091 kg s^{-1}, meridional tracer flux = 537 kg s^{-1}) but the ratio is the same (0.67).

Southward tracer flux across the midbasin f/h contours is calculated by finding the velocity normal to the f/h contour at each grid point, multiplying it with the tracer concentration at that location and integrating along the f/h contour from the western boundary to the eastern boundary (as opposed to the above calculations where the integration was only over the westernmost 200 km of the basin). Time series of southward tracer flux (Fig. 8) show that tracer is transported southward during specific events (especially in the flat-bottom configuration).

In the remainder of this section, we will examine the mechanisms important to the flux of tracer across the midbasin f/h contour. In related work, Figueroa (1994) examines the tracer transport mechanisms important in the surface layer for mixing tracer across a zonal jet. He describes three main mechanisms: the subgrid-scale diffusion, the formation and shedding of rings transporting tracer anomalies across the front, and a phase

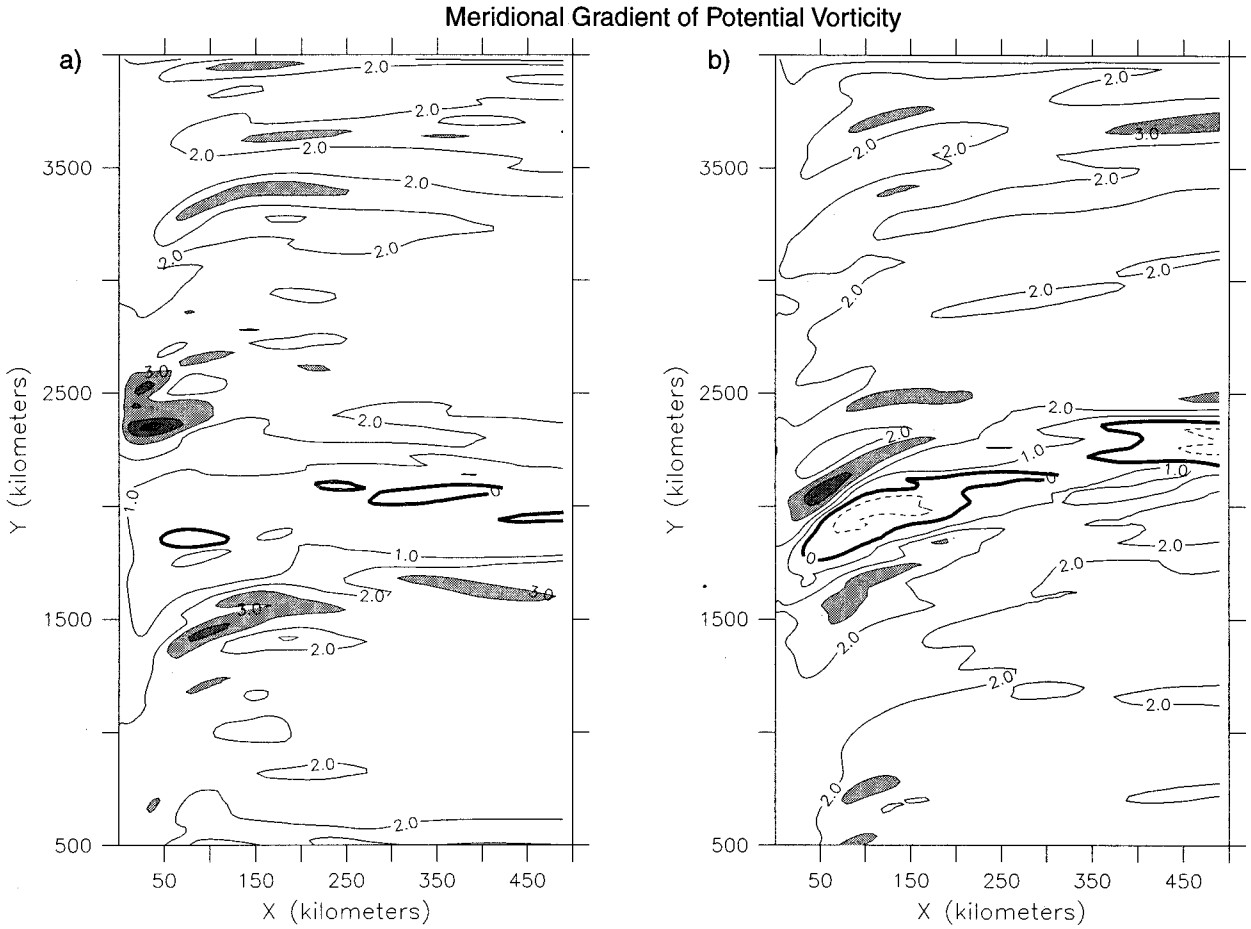

FIG. 6. Meridional derivative of time averaged potential vorticity (contour interval = 1.0×10^{-11} m^{-1} s^{-1}). For (a) flat-bottom configuration and (b) topography configuration. Values greater than 3.0×10^{-11} m^{-1} s^{-1} are shaded.

shift between meandering streamlines and tracer isopleths. The primary difference between the work presented here and Figueroa (1994) is that we examine tracer transport mechanisms in the abyss where there is no coherent jet that the tracer has to cross. The instantaneous streamfunction (Fig. 9) shows the surface jet in layers one and two. However, no coherent remnant of the surface jet exists in the third layer. Therefore, we examine the flux of tracer across the aforementioned midbasin f/h contour instead of across a jet. We find that mean meridional transport by the DWBC is of primary importance, while eddies (or rings as in Figueroa) play a secondary but still important role.

In order to study the mechanisms important to tracer transport across this midbasin barrier, several of the tracer transport events are examined in detail. First the tracer transport mechanisms in the flat-bottom case are discussed. Tracer transport events are defined as periods when the maximum tracer transport is greater than 4000 kg s^{-1}. Using this definition, ten events are recognized over the 5000-day model run (see Fig. 8). These ten events carry 10%–15% (roughly half of the eddy contribution) of the total meridional tracer flux across midbasin. An examination of the ten events reveals one feature that is common to all. The tracer transport event that occurs around day 904 (event 2 of Fig. 8) of the flat-bottom model run provides a nice example. The cyclonic eddy seen in the streamfunction contours (Fig. 10) at the western boundary between $y = 1900$ km and $y = 2300$ km is a feature common to all ten of the tracer transport events that were examined. During periods of low tracer transport, the cyclonic eddy is generally not there at all, is much weaker, or occurs farther north or farther south than during tracer transport events. Thus, it seems that the presence of a cyclonic eddy at midbasin on the western boundary is necessary in order to push a pulse of tracer across the f/h barrier.

The cyclonic eddy enhances the southward component of velocity in the DWBC. The southward component of velocity averaged over the westernmost 50 km at midbasin ($y = 2000$ km) was calculated both as an average over the ten tracer transport events and as an average over the entire model run. This component of velocity during tracer transport events averages 27

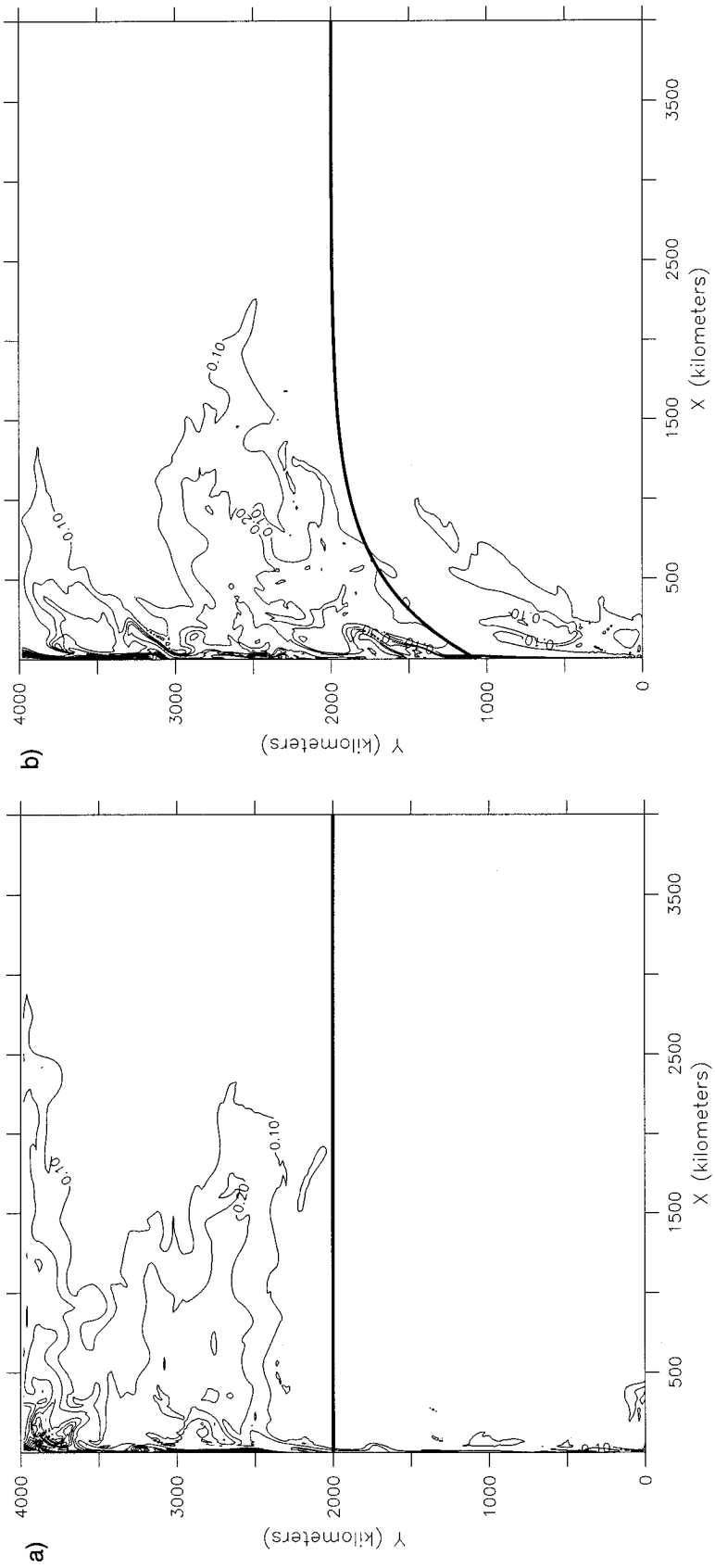

FIG. 7. Contours of tracer concentration at the end of a 5000-day model run (contour interval = 0.1 kg m^{-2}) for (a) flat bottom and (b) topography. Dark line is the midbasin f/h contour.

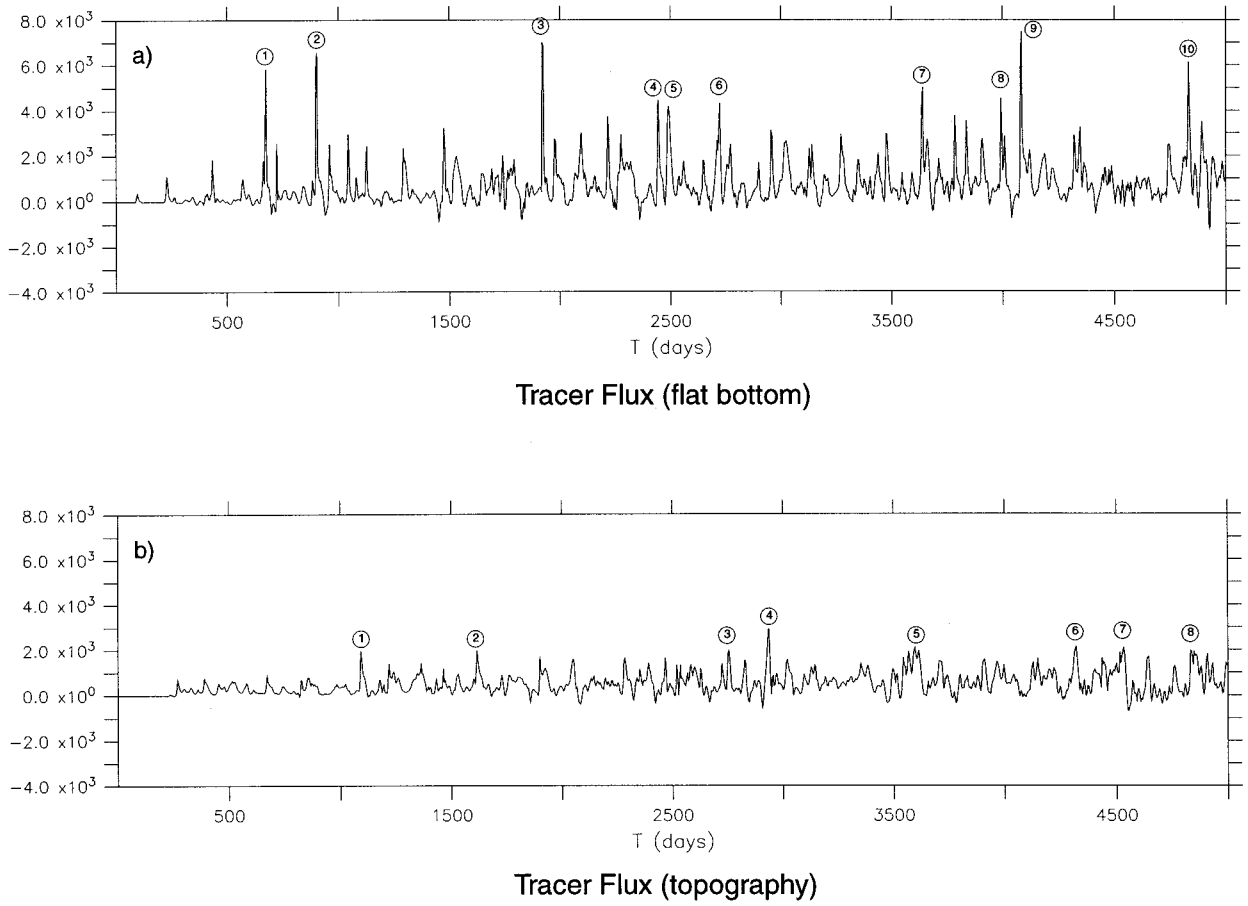

FIG. 8. Time series of southward tracer flux across the midbasin f/h contour (units in kg s^{-1}) for (a) flat bottom and (b) topography.

cm s^{-1} as compared to an average over the entire model run of 15 cm s^{-1}. Thus, the cyclonic eddies seen during tracer transport events almost double the southward speed of the DWBC. For comparison, mean DWBC speeds measured with current meters are approximately 5–10 cm s^{-1} (e.g., Luyten 1977), while typical synoptic velocity estimates give approximately 20 cm s^{-1} (e.g., Joyce et. al. 1986).

Contours of tracer concentration (Figs. 10e–h) show a blob of tracer crossing midbasin during day 904. Once the blob of tracer crosses the midbasin line, it breaks off from the main concentration of tracer and continues southward along the western boundary. The other tracer transport events also exhibit this bloblike character.

When topography is introduced, the tracer transport picture becomes more complicated. The amount of the total meridional tracer transport is only about 72% of that for the flat-bottom case and the magnitude of the events is also quite a bit smaller (see Fig. 8), making it more difficult to define tracer transport events. Defining tracer transport events as those periods of time during which the tracer transport exceeds 1900 kg s^{-1} results in eight events over the 5000-day model run. The velocity component normal to the f/h contour averaged over the westernmost 50 km of the basin was calculated. Averaged over the eight events, this velocity is 20 cm s^{-1} as compared to a mean for the entire run of 17 cm s^{-1}. Thus, the events in the topography configuration are not as distinct from the mean as they were in the flat-bottom configuration. In fact, when comparing the streamfunction fields of high transport periods with those of low transport periods, it is difficult to see any consistent differences. There appears to be a subtle difference in the orientation of the eddies. The periods of high meridional tracer flux (Fig. 11 shows event 2 of Fig. 8 as an example) across the midbasin f/h contour seem to occur when the eddies along the western boundary have more of a north–south orientation. During low tracer flux periods (Fig. 12), the eddies are more likely to be oriented to follow contours of f/h. Because the eddies are stretched out to follow f/h contours, they serve to entrain tracer-poor interior water into the DWBC. This entrainment of interior water is one likely cause of the dramatic change in water properties south

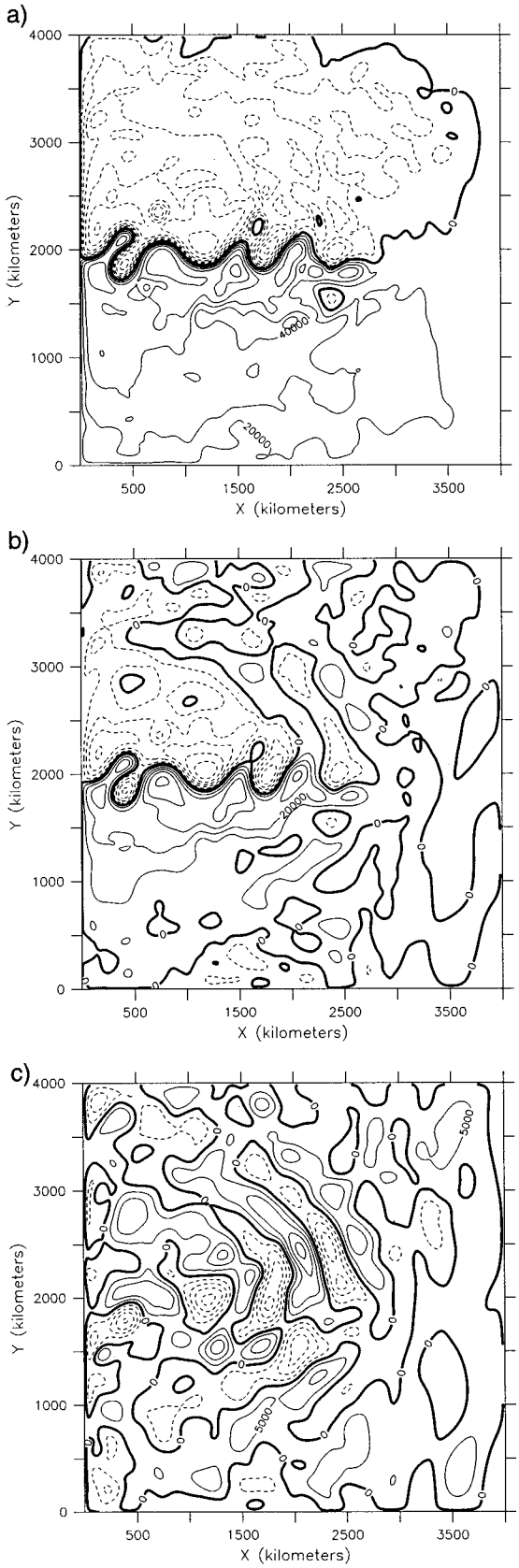

of the Gulf Stream crossover seen by Pickart and Smethie (1993).

The southward tracer flux across the midbasin f/h contour can be broken into mean and eddy quantities:

$$\int_{0\,\mathrm{km}}^{200\,\mathrm{km}} \overline{(\mathbf{v}T)}\cdot\mathbf{n}\,ds = \int_{0\,\mathrm{km}}^{200\,\mathrm{km}} (\overline{\mathbf{v}}\,\overline{T})\cdot\mathbf{n}\,ds + \int_{0\,\mathrm{km}}^{200\,\mathrm{km}} \overline{(\mathbf{v}'T')}\cdot\mathbf{n}\,ds, \quad (1)$$

where $\mathbf{v}\cdot\mathbf{n} = (\overline{\mathbf{v}} + \mathbf{v}')\cdot\mathbf{n}$ is the component of velocity normal to the f/h contour, $T = \overline{T} + T'$ is tracer concentration at the f/h contour, and ds is along the f/h contour. The overbar denotes a time average (in this case over the final 4000 days of the model run), and the prime denotes the departure from the time mean. The first term on the right-hand side of (1) is a measure of the amount of tracer flux due to the mean flow field, while the second term is flux due to the time-dependent eddy field. In the flat-bottom case, the total meridional tracer flux across the f/h contour averaged over the final 4000 days of the model run is approximately 740 kg s^{-1}. This total is made up of 611 kg s^{-1} (83%) due to the mean flow field and 129 kg s^{-1} (17%) due to the eddy field. In the topography case, a total flux of 537 kg s^{-1} is made up of 524 kg s^{-1} (98%) due to the mean flow field and 12 kg s^{-1} (2%) due to the eddy field. These numbers confirm the conclusion drawn above that the eddy field is more important in the flat-bottom case (accounting for almost 20% of the meridional tracer flux) and much less important in the topography case (accounting for only 2%).

Note that this analysis does not take into account the extent to which the mean flow field is driven by the eddies. In order to get a measure of the effect of the eddies on the mean flow field, a run was made with the wind turned off. Thus, the only forcing was the DWBC inflow. Without the wind, there are no instabilities to drive eddy formation. Because the eddies add a large zonal component to the mean flow field, a model run with zero wind results in almost zero zonal flux of tracer into the interior. All of the tracer remains in the boundary current and crosses the f/h contour into the southern half of the basin. Therefore, the mean meridional tracer flux of 740 kg s^{-1} noted above is only about 20% of what it would be without any eddies at all.

c. Zonal tracer flux

With an active eddy field and a source of tracer in the western boundary, tracer must be transported zonally

←

FIG. 9. Example of instantaneous streamfunction fields for the flat-bottom configuration. (a) Layer 1 (contour interval = 20 000 $m^2\,s^{-1}$); (b) layer 2 (contour interval = 10 000 $m^2\,s^{-1}$); (c) layer 3 (contour interval = 5000 $m^2\,s^{-1}$).

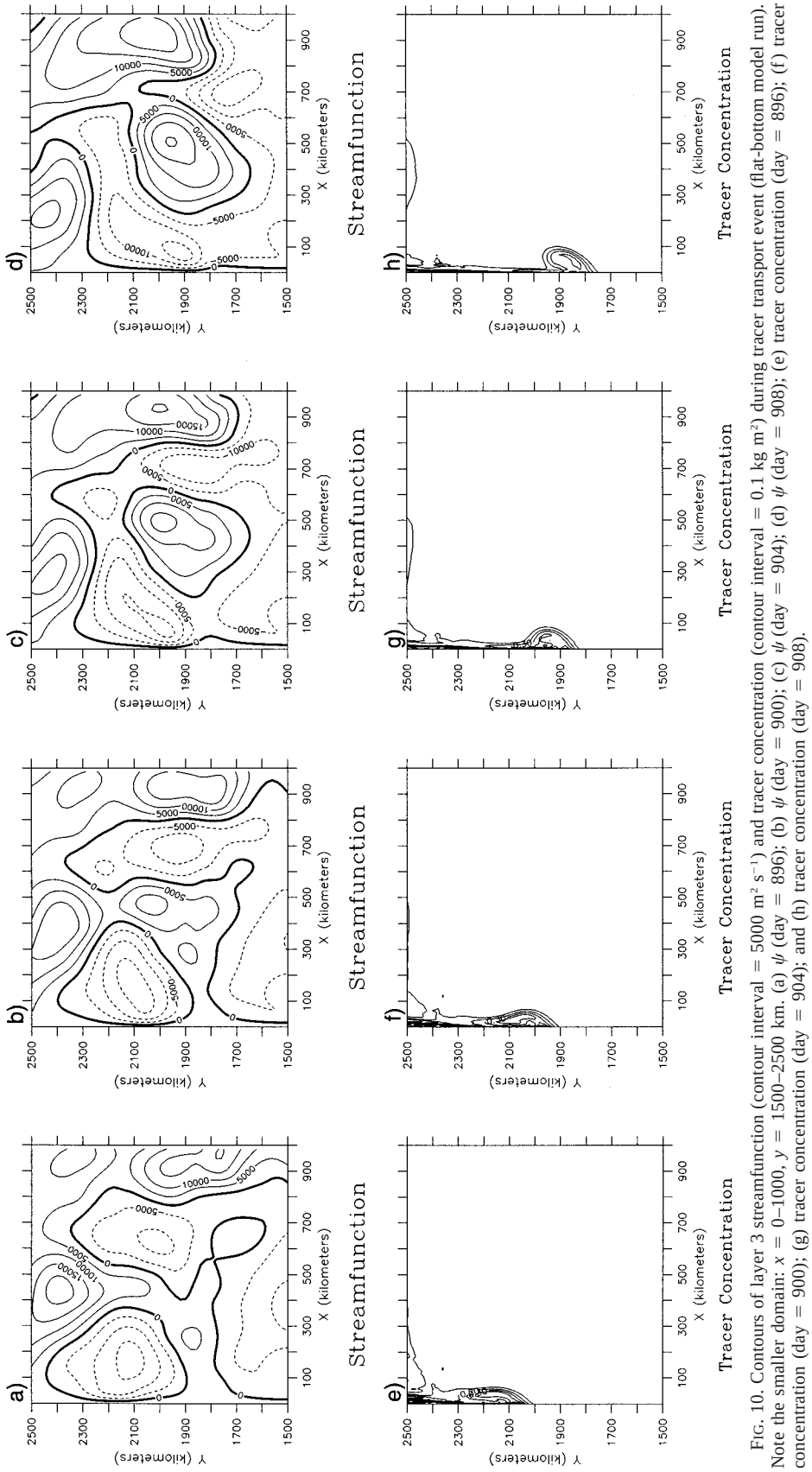

FIG. 10. Contours of layer 3 streamfunction (contour interval = 5000 $m^2 s^{-1}$) and tracer concentration (contour interval = 0.1 kg m^2) during tracer transport event (flat-bottom model run). Note the smaller domain: x = 0–1000, y = 1500–2500 km. (a) ψ (day = 896); (b) ψ (day = 900); (c) ψ (day = 904); (d) ψ (day = 908); (e) tracer concentration (day = 896); (f) tracer concentration (day = 900); (g) tracer concentration (day = 904); and (h) tracer concentration (day = 908).

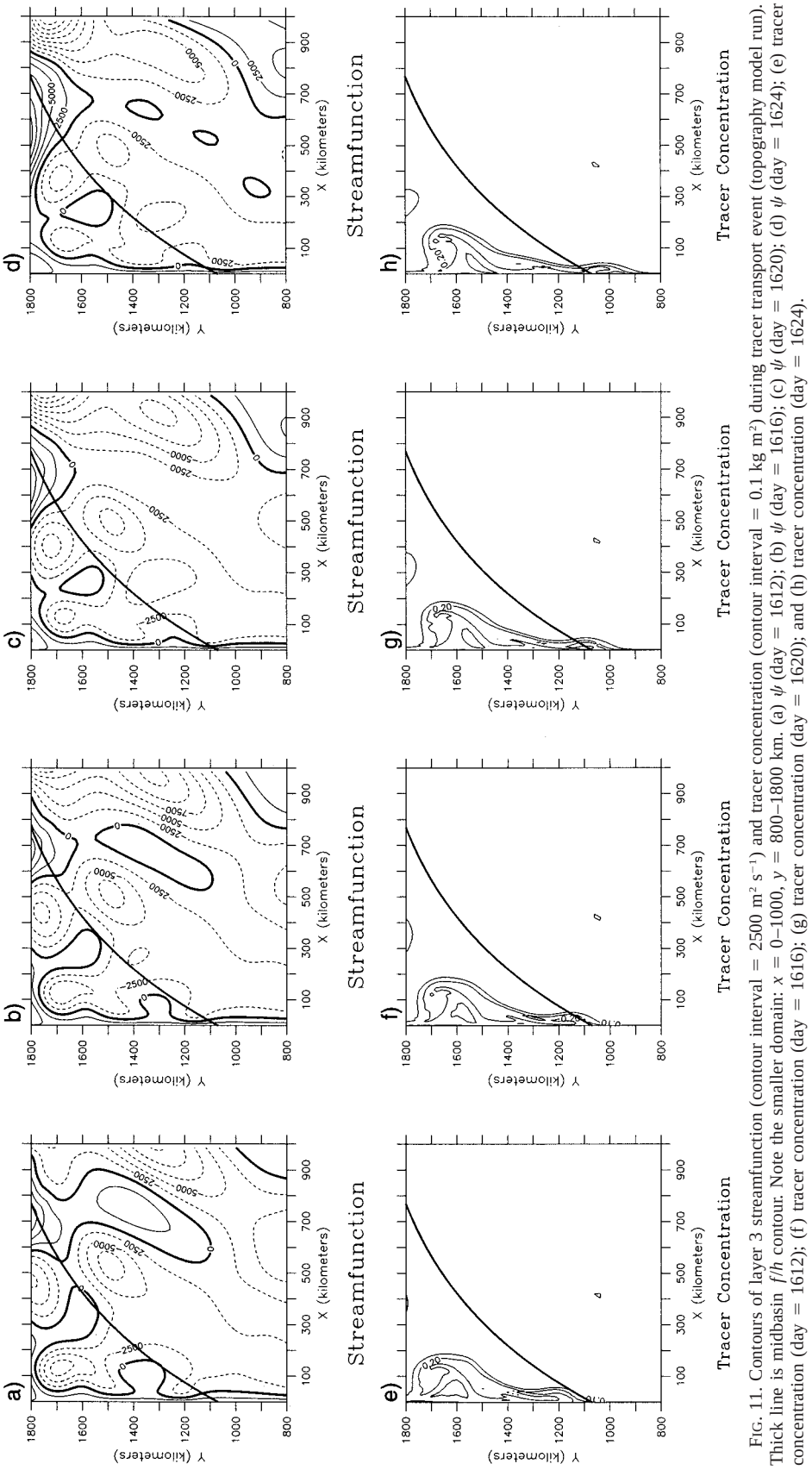

FIG. 11. Contours of layer 3 streamfunction (contour interval = 2500 $m^2 s^{-1}$) and tracer concentration (contour interval = 0.1 kg m^2) during tracer transport event (topography model run). Thick line is midbasin f/h contour. Note the smaller domain: x = 0–1000, y = 800–1800 km. (a) ψ (day = 1612); (b) ψ (day = 1616); (c) ψ (day = 1620); (d) ψ (day = 1624); (e) tracer concentration (day = 1612); (f) tracer concentration (day = 1616); (g) tracer concentration (day = 1620); and (h) tracer concentration (day = 1624).

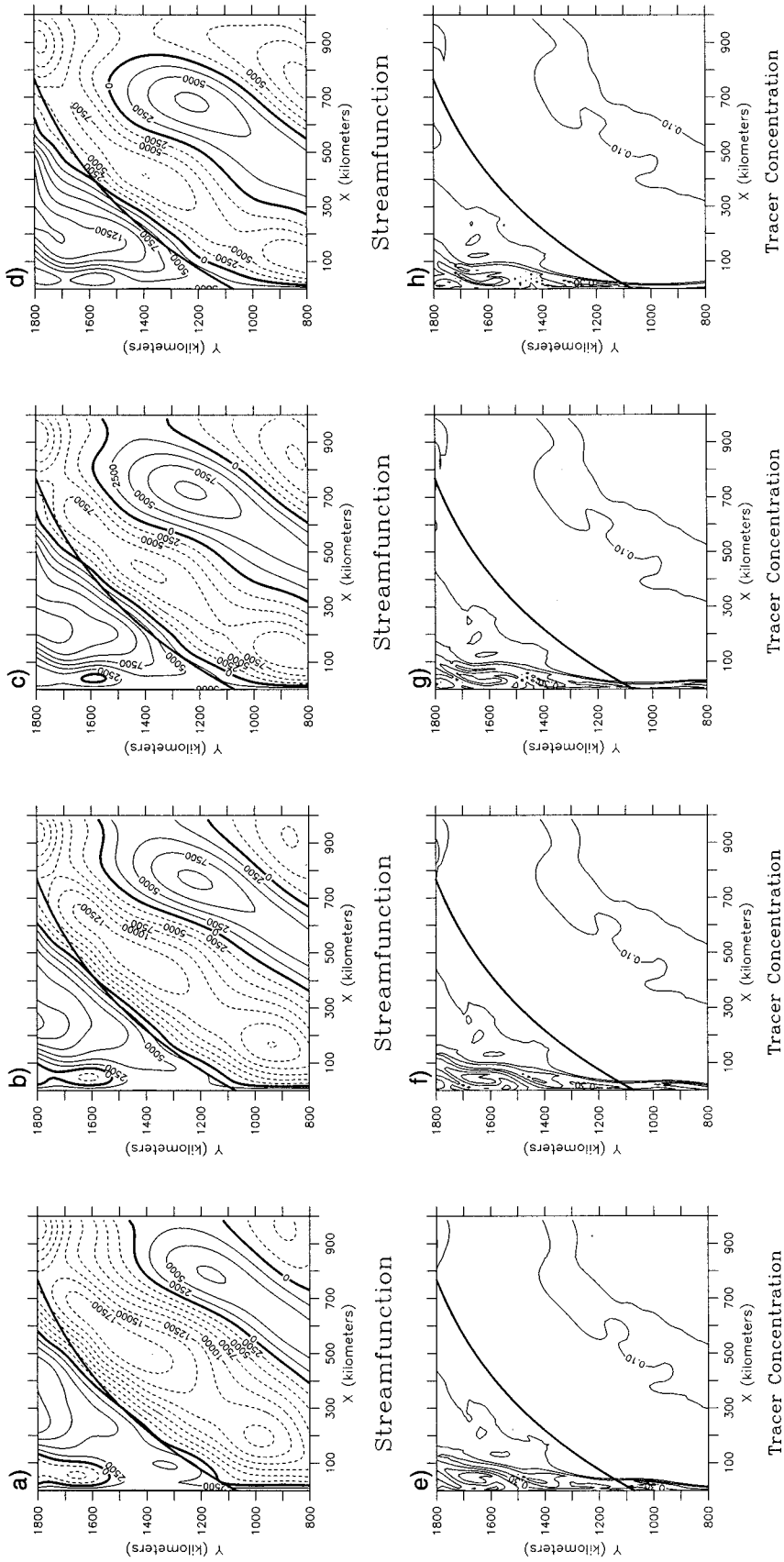

FIG. 12. Contours of layer 3 streamfunction (contour interval = 2500 m^2 s^{-1}) and tracer concentration (contour interval = 0.1 kg m^2) during period of low tracer transport (topography model run). Thick line is midbasin f/h contour. Note the smaller domain: x = 0–1000, y = 800–1800 km. (a) ψ (day = 4552); (b) ψ (day = 4556); (c) ψ (day = 4560); (d) ψ (day = 4564); (e) tracer concentration (day = 4552); (f) tracer concentration (day = 4556); (g) tracer concentration (day = 4560); and (h) tracer concentration (day = 4564).

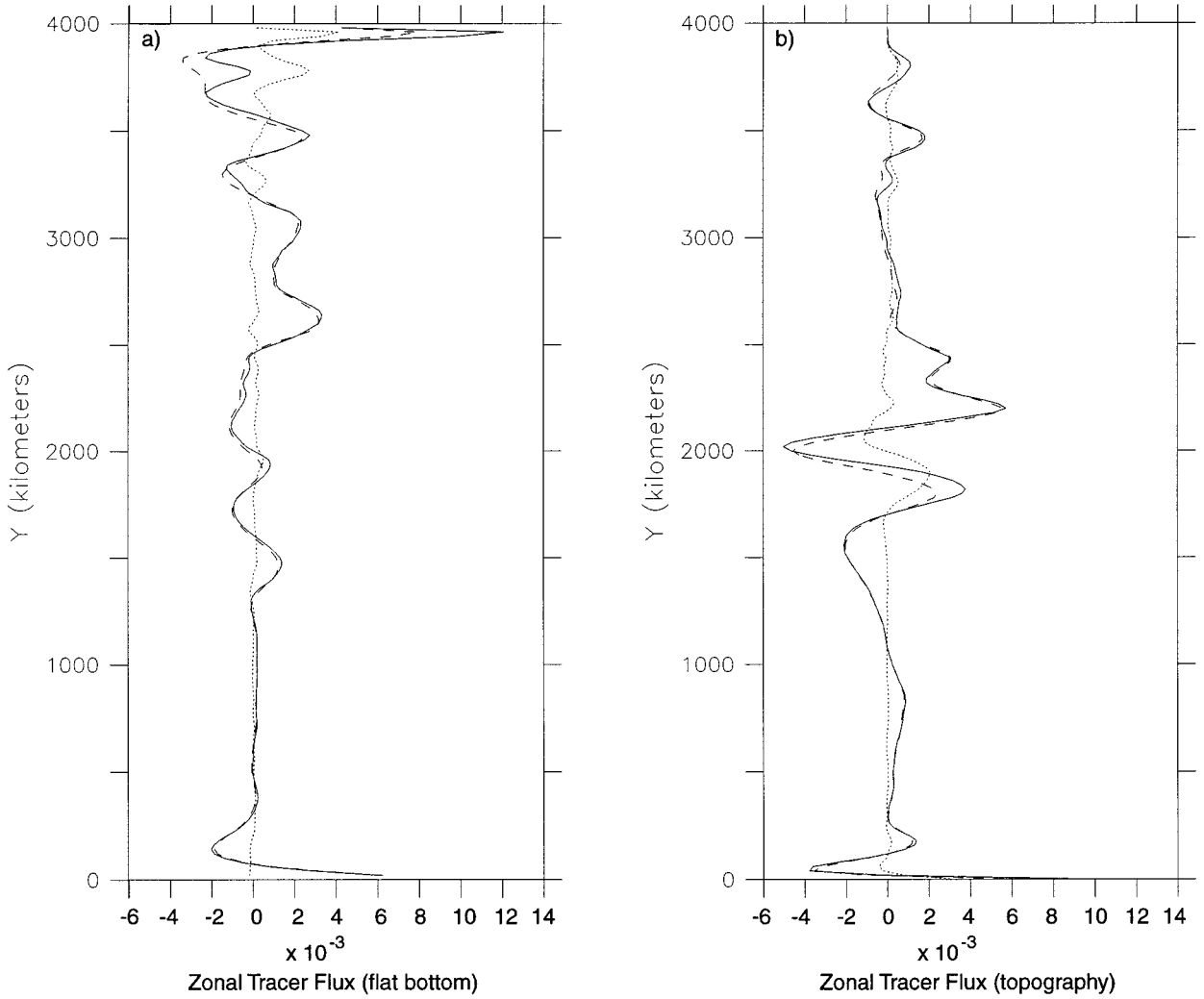

FIG. 13. Zonal tracer flux versus latitude (averaged over final 4000 days of the 5000-day model run). Solid line corresponds to term 1 of Eq. (1) in text; dashed line: term 2; dotted line: term 3. (a) Flat bottom; (b) topography.

into the interior as well as meridionally. Initially there is no tracer in the interior of the basin. The eddies pick up tracer-rich water in the western boundary and transport it to the tracer poor interior. As the eddies grow and decay, they leave behind tracer-laden water in the interior. In addition, any zonal mean recirculation that passes through the boundary current would also bring tracer into the interior.

As mentioned previously, the zonal tracer flux across $x = 200$ km into the interior accounts for approximately 70% of the flux out of the northern part of the boundary current, the other 30% being the flux of tracer to the southern part of the basin in the boundary current. The mean streamfunction (Figs. 2 and 3) shows very weak recirculations in the northern part of the third layer (i.e., $y > 3000$ km for the flat-bottom configuration and $y > 2500$ km for the topography configuration). However, even in these northernmost regions of the model basin, tracer gets into the interior (Fig. 7). Thus, the eddy field must be at least partially responsible for moving tracer into the interior in this region. Using (1), we can confirm this speculation by estimating the contributions of the mean and the eddy flow fields to the zonal tracer flux.

In the flat-bottom case, the total time-mean zonal flux of tracer into the interior is about 1533 kg s^{-1} of which 877 kg s^{-1} (57%) is due to the mean flow field and 655 kg s^{-1} (43%) is due to the eddy flow field. In the topography case the total zonal flux of tracer into the interior is about 1091 kg s^{-1} of which 651 kg s^{-1} (60%) is due to the mean flow field and 440 kg s^{-1} (40%) is due to the eddy flow field. Thus, as expected, the eddy field is important to the zonal flux of tracer into the interior.

However, the importance of the eddy field to zonal tracer flux is quite dependent on latitude (Fig. 13). In the flat-bottom case, south of approximately $y = 3500$

km, the total zonal tracer transport is primarily due to the mean flow. In addition, the majority of the eastward tracer flux occurs in the range 2500 km $< y <$ 3000 km. In the topography case, the majority of the zonal tracer flux (and the place where the eddies make a contribution) occurs in the range 1500 km $< y <$ 2500 km. These regions of enhanced zonal tracer transport are consistent with the mean streamfunction (Figs. 2 and 3), the shape of the tracer envelope after 5000 days (Fig. 7), and the region of enhanced meridional potential vorticity gradient (Fig. 6).

d. Lateral dissipation

Lateral dissipation of potential vorticity in the model is parameterized as Laplacian friction (following Lozier and Riser 1989). The choice of Laplacian friction, rather than biharmonic friction, to model subgrid-scale dissipation was made to simplify the boundary conditions of the model. In order to test the dependence of the results of this study on the lateral dissipation coefficient, two additional 1000-day model runs (after spinup) with different coefficients were made for comparison. The results of the central case, with a lateral dissipation coefficient of $\nu = 100$ m^2 s^{-1} form the basis of this study. This value is consistent with the lateral diffusivity coefficient deduced by Pickart and Hogg (1989). The two additional runs have coefficients of $\nu_1 = 50$ m^2 s^{-1} and $\nu_2 = 500$ m^2 s^{-1}.

Decreasing the lateral dissipation coefficient by a factor of 2 (ν versus ν_1) does not substantially change our results. The mean streamfunction fields (Fig. 2 shows the mean streamfunction for the central case; the mean streamfunction for ν_1 is not shown) look quite similar, especially in the second and third model layers. The main difference in the mean flow field in the surface layer is that the surface jet does not reach as far into the interior with coefficient ν_1. In addition, the meridional and zonal tracer fluxes were calculated for comparison. The character of the meridional tracer flux during the 500-day period from day = 500 to day = 1000 looks quite similar between the two cases: The magnitude of the tracer transport events is similar and the breakdown of the eddy versus mean contributions to the total meridional tracer flux is also roughly the same (54% due to the mean for ν, compared with 60% for ν_1). The zonal tracer fluxes also look similar in magnitude and mean versus eddy breakdown although the peak in zonal tracer flux occurs approximately 400 km north of that for the central case. In addition, the spatial scales of the eddies are quite similar between the two cases. Because these results are so similar, we feel that for a reasonable range of lateral dissipation coefficients, the results of this study are not highly dependent on this parameter.

Increasing the lateral dissipation coefficient by a factor of 5 (ν versus ν_2), on the other hand, does have a substantial impact on the dynamics of the abyssal layer. The mean streamfunction in the third layer becomes less eddy-driven and much more dominated by the DWBC. The damping of the eddies by the large dissipation coefficient is also reflected in the breakdown of the eddy versus mean contributions to the total meridional tracer flux. With $\nu_2 = 500$ m^2 s^{-1}, the mean contribution accounts for 96% of the total meridional tracer flux. The results for this large lateral dissipation coefficient approach the non-eddy-resolving regime discussed in section 3e.

Although the eddies depend on the frictional parameterization, the results of this study primarily depend on the interplay between the eddies and the frictionally dominated western boundary current. If we were to use a different frictional parameterization, the structure of the boundary layer would be different but we believe that our results would be qualitatively similar. In addition, having a more complex boundary layer structure (as we would with biharmonic friction) is not necessarily more realistic.

e. Eddy diffusivity parameterization

Eddies play a role in tracer flux on two levels: 1) the direct influence of the eddies in transporting tracer and 2) the effect of the eddies in driving the mean flow. As discussed in sections 3b and 3c, the mean flow transports the majority of the tracer both meridionally and zonally and the strength of the eddy flux of tracer depends on whether the model includes variable topography along the western boundary. However, the effect of the eddies in driving the mean flow has a large impact on tracer fluxes. Thus, one way or the other, eddies play a role in the flux of tracer both meridionally and zonally.

In order to resolve the eddies, the resolution of this model is fairly high (minimum grid spacing of 4 km at western boundary and maximum grid spacing of 20 km in the interior). Thus, the model runs presented here are computationally expensive. An important question is whether we can reduce the resolution and parameterize the eddies in such a way as to reproduce the important results of the eddy-resolving model.

In a pair of papers, Figueroa and Olson (1994) and Figueroa (1994) address this question for the surface ocean. Using numerical float dispersion in an eddy-resolving double-gyre model, they estimate both an anisotropic eddy diffusivity field using Taylor's (1921) classic diffusion theory and an isotropic, spatially varying ''deformation dependent'' field based on work by Smagorinsky (1963). In related work, Böning and Cox (1988) used particle dispersion in a model of the eastern part of a gyre to estimate eddy diffusivities ($\kappa_{xx} = 8 \times 10^7$ cm^2 s^{-1}, $\kappa_{yy} = 3 \times 10^7$ cm^2 s^{-1}); Colin de Verdiere (1983) estimated diffusivities from surface drifters in the eastern North Atlantic ($\kappa_{xx} = 2.3 \times 10^7$ cm^2 s^{-1}, $\kappa_{yy} = 1.7 \times 10^7$ cm^2 s^{-1}); and Freeland et al. (1975) estimated diffusivities from SOFAR floats at 1500 m in the Sargasso Sea ($\kappa_{xx} = 7.8 \times 10^6$ cm^2 s^{-1}, $\kappa_{yy} = 7.1$

$\times 10^6$ cm^2 s^{-1}). Figueroa and Olson (1994) compute eddy diffusivities by region and they find that the diffusivity in the region of the free jet can be up to two orders of magnitude higher than in the interior.

Figueroa (1994) then uses the estimates of eddy diffusivity calculated by Figueroa and Olson (1994) to compare the evolution of a passive tracer in a high-resolution model with that in a simulated course-resolution model that includes eddy diffusivity, [''simulated'' because Figueroa (1994) uses the mean velocity field from the high-resolution model runs to represent a coarse-resolution velocity field]. He finds that no eddy diffusivity field can completely reproduce the tracer distribution and the meridional tracer fluxes seen in the high-resolution model runs. However, he also finds that the use of a spatially dependent horizontal diffusivity field greatly improves the results over the use of a constant eddy diffusivity.

In this paper, we explore some of the same questions for the case of a tracer-laden DWBC. In addition to using the high-resolution mean streamfunction (which includes the eddy driven component of the mean flow) to represent a course-resolution model as in Figueroa (1994), we also run some tests using an actual low-resolution streamfunction. The advantage to the first approach is that it guarantees that the mean circulation in the high and the simulated-low resolution runs is the same. This aids in comparison between the two runs as any differences in tracer concentrations are due solely to differences between the actual effects of eddies and the effects of eddy diffusivity. However, the mean streamfunction from the high-resolution model runs does not look much like the streamfunction from a low-resolution run. Therefore, the second approach, using the mean streamfunction from an actual low (100-km grid spacing) resolution run, is also done.

Because the low-resolution model streamfunction in the lower layer (Fig. 14) approaches the linear limit at which meridional spatial scales are very large compared to zonal spatial scales, the inclusion of topography makes very little difference. Therefore, only the flat-bottom case will be discussed here. In the linear limit, the western boundary layer can be estimated with a boundary layer in which potential vorticity input by the wind is dissipated by lateral friction. The zonal length scale of the boundary layer is $\delta = (\nu/\beta)^{1/3}$, where δ is the zonal length scale, ν is the lateral dissipation coefficient, and β is the meridional gradient of the Coriolis parameter. In the high-resolution model, δ is on the order of 20 km. When the resolution is reduced to 100-km grid spacing, ν has to be increased in order for the model to remain stable. In the low-resolution model runs, ν is increased to 20 000 m^2 s^{-1}, making δ equal to 100 km. As compared to the high-resolution mean streamfunction, in which the upper layers have a fairly large effect on the bottom layer (Fig. 2), the third layer velocity field in the low-resolution case (Fig. 14) consists only of the imposed DWBC and a meridional recirculation.

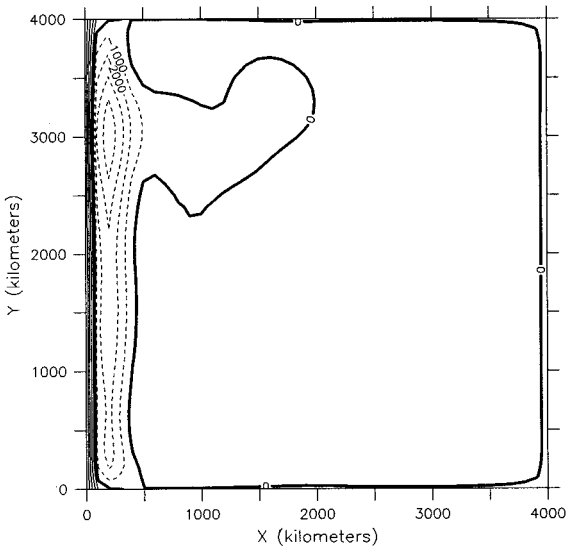

FIG. 14. Time-averaged streamfunction field for the third layer of the low-resolution model (flat-bottom configuration). Grid spacing = 100 km in both x and y (contour interval = 1000 m^2 s^{-1}).

In all eddy diffusivity runs, the boundary conditions are set to create the same tracer influx as in the eddy-resolving model runs and to allow no diffusive flux of tracer out of the basin.

Three different formulations for eddy diffusivity are tested. The first, and simplest, formulation is a constant eddy diffusivity:

$$\kappa = 1070 \text{ m}^2 \text{ s}^{-1}. \quad (2)$$

This value is chosen to correspond to the magnitude of (3) below and is in the range calculated in the studies mentioned above. For numerical stability reasons, κ has to be at least 70 m^2 s^{-1} everywhere.

The second formulation is a spatially varying eddy diffusivity of the form

$$\kappa(x, y) = A + B \exp\left[-\frac{x}{L} - \left(\frac{y - 2000 \text{ km}}{L}\right)^2\right], \quad (3)$$

(a Gaussian in y and a decaying exponential in x). This formulation is an attempt, using a fairly simple formulation, to make the diffusivity high where the eddies are the strongest—at midbasin along the western boundary. The ''deformation dependent'' eddy diffusivity field estimated by Figueroa and Olson (1994) looks much like this. We are making an assumption that the basic form of eddy diffusivity calculated by Figueroa and Olson carries to the layers below. However, this assumption is supported by the fact that the eddy kinetic energy (not shown) that we calculate for the deep layer is quite similar in form (if not in magnitude) to that calculated for the surface ocean by Figueroa and Olson (1994). Results shown here have $A = 70$ m^2 s^{-1}, $B = 1000$ m^2 s^{-1}, and $L = 500$ km.

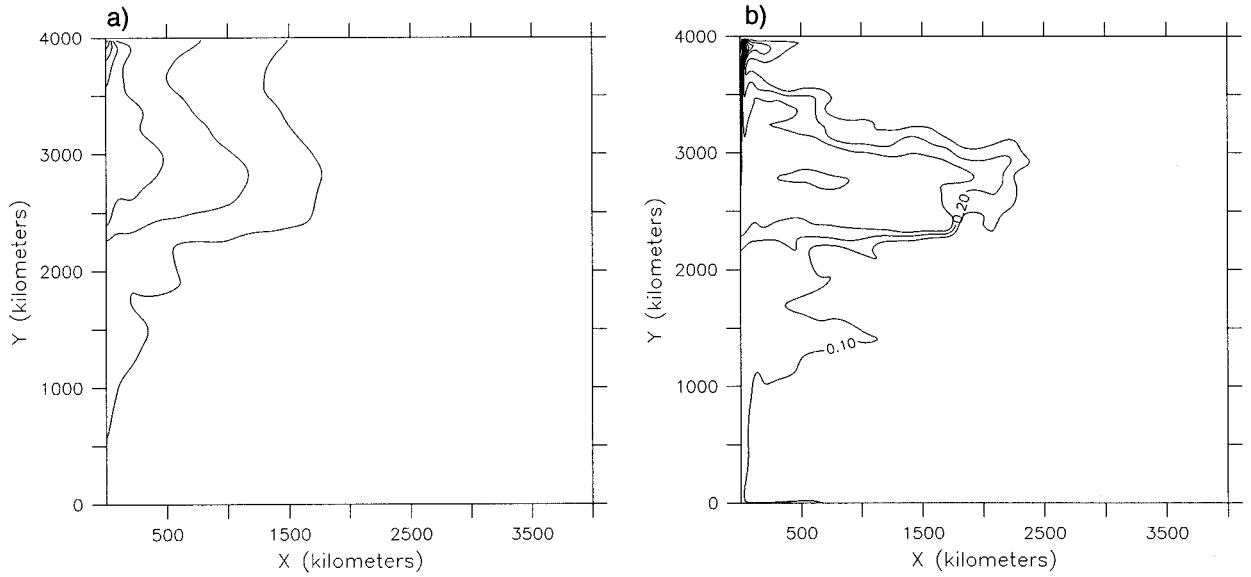

FIG. 15. Contours of tracer concentration (contour interval = 0.1 kg m^2) after being advected by the high-resolution mean streamfunction for 5000 days for (a) constant eddy diffusivity [Eq. (2) in the text] and (b) spatially varying eddy diffusivity [Eq. (3)].

The third formulation tested is an anisotropic eddy diffusivity:

$$\underset{\approx}{\kappa} = \begin{bmatrix} \kappa_{xx} & \kappa_{xy} \\ \kappa_{yx} & \kappa_{yy} \end{bmatrix}, \tag{4}$$

in which the κ_{xx} and the κ_{yy} terms have the same form as (3) but with different magnitudes. In the results shown here, the magnitude of the exponential term in the diffusivity is ten times greater in the x direction than in the y direction. Figueroa and Olson (1994) find differences of up to two orders of magnitude between κ_{xx} and κ_{yy}. For ease of computation, the off-diagonal terms (which account for the tendency of a parcel of tracer to rotate), κ_{xy} and κ_{yx}, are set equal to zero. This is not consistent with findings by Figueroa and Olson (1994). They find that the off-diagonal terms have both positive and negative values that are of the same order of magnitude as the diagonal terms. However, based on our findings with the κ_{xy} and κ_{yx} terms set to zero, we believe that our conclusions would not be appreciably different with nonzero off-diagonal terms.

TABLE 2. Percentage of total tracer in different regions of the model domain after 5000-day model run.

	Model run		
	x = 0–500 km y = 2000–4000 km (Northern DWBC)	x = 500–4000 km y = 200–4000 km (Northern interior)	x = 0–4000 km y = 0–2000 km (Southern half)
Eddy resolving	27%	54%	19%
High resolution			
constant κ	30%	48%	22%
variable κ	26%	54%	20%
Low resolution			
constant κ	32%	26%	42%
variable κ	40%	16%	44%
anisotropic κ	35%	39%	26%

The tracer advection model was run for 5000 days using the high-resolution mean streamfunction and eddy diffusivities (2) and (3) (Fig. 15). In both cases, the midbasin barrier to meridional tracer transport is reproduced. This is due to the fact that the barrier is seen in the high-resolution mean streamfunction (Fig. 2). The fairly successful reproduction of the midbasin barrier can be demonstrated by examining the amount of tracer in three different regions: the northern DWBC (x = 0–500 km, y = 2000–4000 km), the northern interior (east of x = 500 km and north of y = 2000 km), and the southern half of the basin (south of y = 2000 km) (Table 2). At the end of a 5000-day run, the eddy-resolving model results in only 19% of the total tracer burden reaching the southern half of the basin. With a constant eddy diffusivity (2), the amount of tracer in the southern half of the basin after 5000 days is approximately 22%, while using a spatially varying eddy diffusivity (3) results in about 20% of the total tracer burden reaching the southern half of the basin. The amount of tracer in the interior is estimated very accurately by both the constant and the variable diffusivity. The variable diffusivity run is slightly more successful than the constant diffusivity run. The successful reproduction of the midbasin barrier to meridional transport can also be demonstrated by looking at the ratio of zonal transport across x = 200 km to total transport out of the box bounded by x = 200 km on the east and y = 2000 km on the

south. As stated previously, this ratio is about 70% in the eddy-resolving model runs (both flat-bottom and topography). Using the high-resolution mean streamfunction and diffusivities (2) and (3), the resulting ratio is 75%–79%.

Another interesting comparison between the eddy-resolving model and the eddy diffusivity models is the shape of the tracer envelope at the end of the 5000-day runs (Fig. 7a versus Fig. 15). At roughly $y = 2500$ km, the 0.10 kg m^2 tracer concentration contour reaches to approximately $x = 2500$ km into the interior in the eddy-resolving model run (Fig. 7a). The 0.10 kg m^2 tracer concentration contour for the constant eddy diffusivity run only reaches to approximately $x = 2000$ km, and the zonal gradient in tracer concentration is much weaker. However, the variable diffusivity run exhibits a tracer envelope that looks quite similar to that produced by the eddy-resolving run. The tracer reaches approximately the same distance into the interior but the zonal gradient is somewhat greater.

The tracer advection model was also run for 5000 days using the third layer of the low-resolution mean streamfunction and eddy diffusivities (2), (3), and (4), Fig. 16. Only the anisotropic eddy diffusivity run resembles the full high-resolution, time-varying run (Fig. 7a). The midbasin barrier and the zonal tracer flux are not reproduced at all, except when diffusivity (4) is used. When (4) is used, there is some semblance of a barrier at midbasin and more tracer is transported into the interior than in the other two cases. The shape of the tracer envelope for diffusivity (4) (Fig. 16c) has some similarity to the eddy-resolving model run (Fig. 7a). The 0.10 tracer concentration contour reaches approximately $x = 2000$ km into the interior, a vast improvement over eddy diffusivities (2) and (3). However, this contour reaches too far south, showing that the midbasin barrier is too weak. The weakness of the barrier is also demonstrated by the amount of tracer in the southern half of the basin at the end of a 5000-day run: 26% of the total tracer burden compared to 19% for the eddy-resolving run. Also, the amount of tracer in the interior (east of $x = 500$ km and north of $y = 2000$ km) is quite underestimated (39% as opposed to 54% in the eddy-resolving run). Obviously, the form of the eddy diffusivity parameter is important. We could possibly obtain better results with some adjustment of the parameterization [possibly varying A and B in (4) for example]. However, any improvement in the results outlined above would not substantially affect our conclusions.

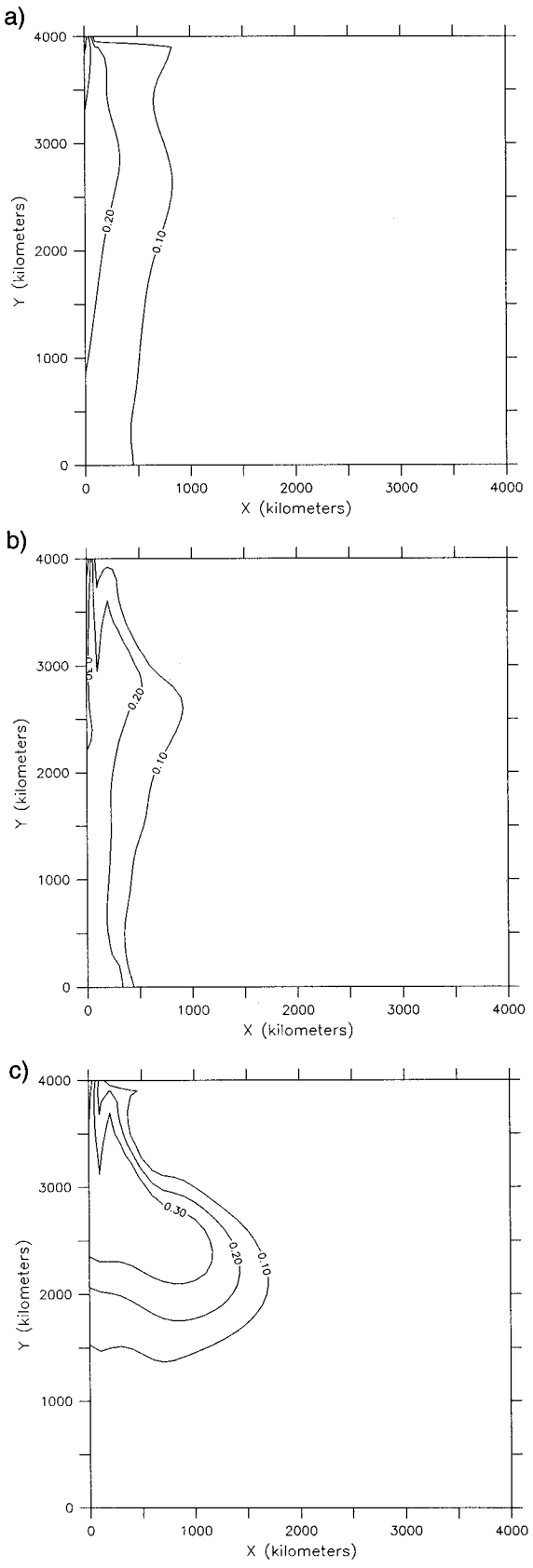

→

FIG. 16. Contours of tracer concentration (contour interval = 0.1 kg m^2) after being advected by the low-resolution mean streamfunction for 5000 days for (a) constant eddy diffusivity [Eq. (2) in the text], (b) spatially varying eddy diffusivity [Eq. (3)], and (c) nonisotropic eddy diffusivity [Eq. (4)].

We conclude that in order to realistically reproduce the effects of eddies, one of two things is needed: either a realistic mean flow field (including the eddy-driven mean flow) or an anisotropic eddy diffusivity formulation. When using a simplistic mean flow (that does not include the eddy-driven mean flow), spatial dependence and anisotropy are important factors in reproducing the effects of eddies on tracer transport. However, because the mean flow accounts for the majority of the tracer transport, a constant eddy diffusivity with a realistic mean flow field may be good enough (depending on the purpose of the model study).

f. Aging

In some model runs, an age tracer is included in the third layer. The aging is initialized with a value of zero everywhere in the model domain and is maintained at a value of zero in the boundary condition that defines the DWBC inflow. In the domain interior, age is advected by the horizontal velocity field and, at each time step, the age is increased by a value equal to the time step size. Thus, the age of the water in the interior, where it has not yet been affected by the DWBC inflow, should be equal to the length of the model run. The equation for the advection of age is

$$\frac{\partial A}{\partial t} + (\mathbf{u}\cdot\boldsymbol{\nabla})A = 1.$$

When used to advect age, the Smolarkiewicz (1983) scheme overcorrects slightly for numerical diffusion, resulting in age values greater than the total age of the model run. Thus, we decided to advect age with a simple upwind advection scheme. Therefore, the advection of age includes more implicit diffusion than the advection of tracer. This difference in advection schemes has very little impact on our results.

By choosing a region in the DWBC, averaging age over that region and calculating the distance of the region from the tracer source, effective velocities can be calculated. This was done for several regions along the length of the DWBC. Interestingly, DWBC velocities derived from age are in the range of 2–3 cm s^{-1}—approximately the same velocity range calculated from tracer observations by Doney and Jenkins (1994) and Pickart et al. (1989). The instantaneous model speeds are on the order of 10–30 cm s^{-1}—in the same range as direct measurements by Pickart and Smethie (1993), Watts (1991), and Fine and Molinari (1988). Spall (1996) found similar results on the effective speeds in the DWBC where it was also shown that the strength of wind forcing, DWBC transport, and the presence of bottom topography can influence the amount of mixing and the effective velocities of the DWBC.

That the model reproduces differences in velocities calculated from age observations versus those from direct measurement is encouraging. It suggests that factors such as mixing, entrainment and detrainment, recirculations, and meanders can account for the differences between velocity estimates. Unless these factors are taken into account, tracer aging can only provide a lower bound for average DWBC advection speeds.

Because of this discrepancy between velocities measured directly and those estimated from tracer age, aging can provide an indicator for regions where mixing and recirculations are important. In the absence of mixing and recirculations, regions with relatively high tracer concentrations should also have a young age. A region with high tracer concentration but older tracer ages is probably a region where mixing and recirculations are important. In a 1000-day model run including tracer advection and aging, the region near the western boundary between $y = 2300$ km and $y = 3000$ km seems to have the most active mixing and recirculations, consistent with the previous discussion on meridional and zonal tracer fluxes.

4. Conclusions

An eddy-resolving quasigeostrophic model is used to investigate the effects of eddies on tracer transport in a southward flowing deep western boundary current as it crosses under an eastward flowing surface jet.

The surface jet creates a dynamical barrier to meridional tracer transport in the DWBC. The model results indicate that the eddy field is responsible for almost 20% of the meridional tracer flux in the flat-bottom case and only 2% in the topography case. This result does not take into account the substantial effect of the eddies in driving the mean flow field.

In the flat-bottom configuration, tracer transport events are triggered by the proximity to the western boundary of cyclonic mesoscale eddies. When topography is introduced, in many cases the presence of a cyclonic eddy near the western boundary impedes meridional tracer transport. Instead, in the topography run, eddies tend to be oriented along curving f/h contours causing entrainment of interior water into the DWBC. Thus, the tracer concentration in the DWBC south of the midbasin f/h contour is much lower than that just north of the midbasin f/h contour.

In addition to the meridional tracer transport in the DWBC, zonal tracer transport is also important. In fact, averaged over the final 4000 days of a 5000-day model run, the ratio of average zonal tracer flux to total tracer flux out of the northern part of the DWBC is approximately 70%. The model shows that tracer is advected and mixed into the interior, even away from the surface jet crossover region. The eddy field is responsible for approximately 40% of the zonal tracer flux into the interior when averaged over the northern half of the basin. However, the dependence of zonal tracer flux on eddies is highly latitude-dependent and in the region of interest (far from the northern boundary), the mean field is responsible for most of the zonal tracer flux.

The model results demonstrate that eddies are im-

portant to the movement of tracer in the DWBC, both through direct eddy fluxes of tracer and through the indirect driving of the mean flow. However, eddy-resolving runs are impractical in many situations. Therefore, eddy diffusivity is commonly used to parameterize the effects of eddies. Various eddy diffusivity formulations are tested to see if reasonable results could be obtained without the full eddy-resolving resolution. Findings suggest that the role of the eddy field in driving the mean flow field is of primary importance. If a mean flow field that includes the effects of eddy-driving is used, various eddy diffusivity formulations can be fairly successful at representing the eddy-resolving case. If a simplistic flow field (that does not include the eddy-driven component) is used, the form of the eddy diffusivity is very important and some formulations reproduce important features of the tracer transport better than others. The anisotropy of the eddy field seems to be an important feature to tracer transport, especially when the mean flow field is less realistic. We conclude that in order to realistically reproduce the effects of eddies, one of two things is needed: either a realistic mean flow field (including the eddy-driven mean flow) or an anisotropic eddy diffusivity formulation that in some sense reflects the eddy-driven mean flow field.

In some model runs, an age tracer is included in the third layer. Mean speeds along the path of the DWBC can be estimated using tracer ages. Model DWBC speeds derived from age are in the range of 2–3 cm s^{-1}, while model speeds calculated at any point in time are on the order of 10–30 cm s^{-1}. A similar discrepancy is also observed between speeds derived from CFC and tritium/helium aging and direct current measurements in the DWBC in the North Atlantic. The discrepancy is due to mixing, entrainment and detrainment of DWBC water with the interior, recirculations, and meanders. Because of this discrepancy, aging can provide an indicator of regions where mixing and recirculations are important.

The results presented here depend on the interplay between the frictionally dominated DWBC and eddies formed by the instability of the surface jet in the interior. We hope that the scales and amplitudes of the eddies are relatively independent of friction. Of more concern is the dynamics that govern the DWBC as a frictionally dominated current. No matter how friction is parameterized, there would still be some question about the realism of the boundary dynamics.

Acknowledgments. We are grateful to W. Holland for helpful discussions in the preparation of this paper. This work was supported by an Office of Naval Research Graduate Fellowship (Ladd) and National Science Foundation Grant OCE-9302170 (Thompson).

REFERENCES

Böning, C. W., and M. D. Cox, 1988: Particle dispersion and mixing of conservative properties in an eddy-resolving model. *J. Phys. Oceanogr.,* **18,** 320–338.

Colin de Verdiere, A., 1983: Lagrangian eddy statistics from surface drifters in the eastern North Atlantic. *J. Mar. Res.,* **41,** 375–398.

Doney, S. C., and W. J. Jenkins, 1994: Ventilation of the deep western boundary current and abyssal western North Atlantic: Estimates from tritium and ^{3}He distributions. *J. Phys. Oceanogr.,* **24,** 638–659.

Figueroa, H. A., 1994: Eddy resolution versus eddy diffusion in a double gyre GCM. Part II: Mixing of passive tracers. *J. Phys. Oceanogr.,* **24,** 387–402.

——, and D. B. Olson, 1994: Eddy resolution versus eddy diffusion in a double gyre GCM. Part I: The Lagrangian and Eulerian description. *J. Phys. Oceanogr.,* **24,** 371–386.

Fine, R. A., and R. L. Molinari, 1988: A continuous deep western boundary current between Abaco (26.5°N) and Barbados (13°N). *Deep-Sea Res.,* **35,** 1441–1450.

Freeland, H. J., P. B. Rhines, and T. Rossby, 1975: Statistical observations of the trajectories of neutrally buoyant floats in the North Atlantic. *J. Mar. Res.,* **33,** 383–404.

Gammon, R. H., and J. Bullister, 1982: Freon penetration into the North Atlantic deep water. *Trans. Amer. Geophys. Union,* **63,** 77.

Hogg, N. G., and H. Stommel, 1985: On the relation between the deep circulation and the Gulf Stream. *Deep-Sea Res.,* **32,** 1181–1193.

Holland, W. R., 1978: The role of mesoscale eddies in the general circulation of the ocean—Numerical experiments using a wind-driven quasi-geostrophic model. *J. Phys. Oceanogr.,* **8,** 363–392.

Jenkins, W. J., and P. B. Rhines, 1980: Tritium in the deep North Atlantic Ocean. *Nature,* **286,** 877–890.

Joyce, T. M., C. Wunsch, and S. D. Pierce, 1986: Synoptic Gulf Stream velocity profiles through simultaneous inversion of hydrographic and acoustic Doppler data. *J. Geophys. Res.,* **91,** 7573–7585.

Lozier, M. S., and S. C. Riser, 1989: Potential vorticity dynamics of boundary currents in a quasi-geostrophic ocean. *J. Phys. Oceanogr.,* **19,** 1373–1396.

Luyten, J. R., 1977: Scales of motion in the Deep Gulf Stream and across the continental rise. *J. Mar. Res.,* **35,** 49–74.

McWilliams, J. C., 1977: A note on a consistent quasigeostrophic model in a multiply connected domain. *Dyn. Atmos. Oceans,* **1,** 417–441.

Pickart, R. S., 1992: Space–time variability of the deep western boundary current oxygen core. *J. Phys. Oceanogr.,* **22,** 1047–1061.

——, 1994: Interaction of the Gulf Stream and Deep Western Boundary Current where they cross. *J. Geophys. Res.,* **99,** 25 155–25 164.

——, and N. G. Hogg, 1989: A tracer study of the deep Gulf Stream cyclonic recirculation. *Deep-Sea Res.,* **36,** 935–956.

Pickart, R. S., and D. R. Watts, 1990: Deep western boundary current variability at Cape Hatteras. *J. Mar. Res.,* **48,** 765–791.

——, and W. M. Smethie Jr., 1993: How does the deep western boundary current cross the Gulf Stream? *J. Phys. Oceanogr.,* **23,** 2602–2616.

——, N. G. Hogg, and W. M. Smethie Jr., 1989: Determining the strength of the deep western boundary current using the chlorofluoromethane ratio. *J. Phys. Oceanogr.,* **19,** 940–951.

Rhein, M., 1994: The Deep Western Boundary Current: Tracers and velocities. *Deep-Sea Res.,* **41,** 263–281.

Rhines, P. B., and R. Schopp, 1991: The wind-driven circulation: Quasigeostrophic simulations and theory for nonsymmetric winds. *J. Phys. Oceanogr.,* **21,** 1438–1469.

Smagorinsky, J. S., 1963: General circulation experiments with the primitive equations. Part I: The basic experiment. *Mon. Wea. Rev.,* **91,** 99–164.

Smethie, W. M., Jr., and S. Trumbore, 1984: Chlorofluoromethanes (F-11 and F-12) in the western North Atlantic Ocean and the deep western boundary undercurrent. *Eos, Trans. Amer. Geophys. Union,* **64,** 1089.

Smolarkiewicz, P. K., 1983: A simple positive definite advection scheme with small implicit diffusion. *Mon. Wea. Rev.,* **111,** 479–486.

Spall, M. A., 1996: Dynamics of the Gulf Stream/deep western boundary current crossover. Part I: Entrainment and recirculation. *J. Phys. Oceanogr.,* **26,** 2152–2168.

Taylor, G. I., 1921: Diffusion by continuous movements. *Proc. London Math. Soc.,* **20,** 196–212.

Thompson, L., 1995: The effect of continental rises on the wind-driven ocean circulation. *J. Phys. Oceanogr.,* **25,** 1296–1316.

Thompson, J. D., and W. J. Schmitz Jr., 1989: A limited-area model of the Gulf Stream: Design, initial experiments, and model–data intercomparison. *J. Phys. Oceanogr.,* **19,** 791–814.

Watts, D. R., 1991: Equatorward currents in temperatures 1.8°–6.0°C on the continental slope in the Mid-Atlantic Bight. *Deep Convection and Deep Water Formation in the Oceans,* P. C. Chu and J. C. Gascard, Eds., Elsevier, 183–196.

Wust, G., 1935: *Die Stratosphare.* Wissenschaftliche Ergebnisse der Deutschen Atlantischen Expedition auf dem Vermessungs- und Forschungsschiff ''METEOR'', 1925–1927, Vol. 6, 109–288.